ISSN 1063-7761, Journal of Experimental and Theoretical Physics, 2018, Vol. 127, No. 1, pp. 79–106. © Pleiades Publishing, Inc., 2018.
Original Russian Text © N.A. Inogamov, V.V. Zhakhovskii, V.A. Khokhlov, 2018, published in Zhurnal Eksperimental'noi i Teoreticheskoi Fiziki, 2018, Vol. 154, No. 1, pp. 92–123.

SOLIDS AND LIQUIDS

Dynamics of Gold Ablation into Water

N. A. Inogamov[a,b,*], **V. V. Zhakhovskii**[a,b], **and V. A. Khokhlov**[a]
[a] *Landau Institute for Theoretical Physics, Russian Academy of Sciences, Chernogolovka, Moscow oblast, 142432 Russia*
[b] *Dukhov Research Institute of Automatics, ul. Sushchevskaya 22, Moscow, 127055 Russia*
**e-mail: nailinogamov@gmail.com*

Received February 19, 2016

Abstract—Using the gold–water pair as an example, we analyze the problems related to an ultrashort laser action on a metallic target submerged in a transparent liquid.

DOI: 10.1134/S1063776118070075

1. INTRODUCTION

Important experiments (see, e.g., [1–3]) on an ultrashort laser optical action began in the 1990s after the appearance of chirp laser sources in the 1980s (see [4, 5] and review [6]). At the first stage in the 1990s, attention was focused on a heat problem. The pump–probe technique [7, 8], where a heating pulse is followed by a probe pulse, was applied. Here, the amplitude of the phase of a reflected probe pulse are determined to calculate refractive index n of the surface heated by a pump pulse when the probe pulse is reflected (thermal reflectance method). Delay τ_{delay} between the pump and probe pulses is known and controlled. As a result, the evolution of the optical parameters of the irradiated target $n(\tau_{\text{delay}})$ is found after the action of the pump pulse. As a result, the action-induced processes in the target can be traced.

Thus, at he first stage, researchers detected (i) transition into the two-temperature ($2T$) state [1–3] predicted in pioneering work [9] and (ii) sharp increase in the electron thermal conductivity in metals at the $2T$ stage, which was called “ballistic transport.” These are the main two achievements of the first stage. The theoretical basis of the experiments in the 1990s was the $2T$ approach with two thermal equations from [9] for the energies of the electron (E_e) and ion (E_i) subsystems,

$$P_e = \text{EHC} - \text{EXC} + S_L, \quad (1)$$

$$P_i = \text{EXC}, \quad (2)$$

$$P = \text{EHC} + S_L, \quad P = P_e + P_i. \quad (3)$$

The set of Eqs. (1) and (2) is written for an immobile substance (density ρ = const), i.e., without hydrodynamic terms. Here, P_e and P_i are the powers of changing the corresponding energies $\rho\partial E_e/\partial t$ and $\rho\partial E_i/\partial t$ per unit volume, EHC is the energy E_e transport in space via electron heat conduction, $\text{EXC} = \alpha(T_e - T_i)$ is the exchange term that connects the electron and ion subsystems, and S_L is the spatial distribution of the laser heating power. As follows from Eq. (3), the set of Eqs. (1) and (2) conserves total energy $\int(P_e + P_i)dx$ after the end of laser pulse S_L, and the integral is taken over the space occupied by the substance.

It is the “ballistic” effect that is thought to exhibit the two-temperature effect, which consists in splitting into two subsystems ((1) and (2)). As a result, true electron thermal diffusivity $\chi_e \approx (1/3)l_e v_e$ (where l_e and v_e are the free path and the characteristic velocity of conduction electrons, respectively, $v_e \sim v_{\text{F}}$, and v_{F} is the Fermi velocity) comes into play, and the heat absorbed by electrons propagates along the electron subsystem [10] at coefficient χ_e. In the one-temperature ($1T$) situation ($T_e \approx T_i = T$), the rate of heat propagation via electron heat conduction depends on the effective electron thermal diffusivity [10],

$$\chi_{1T} \approx \frac{c_e}{c_i}\frac{l_e v_e}{3};$$

that is, a rigid thermal relation between the e and i subsystems according to general heat conduction equation (3) takes place at stage $1T$.

The energy in the experiments performed in the 1990s was low, the increase in temperature T_e due to an ultrashort action was small, and the electron subsystem remained strongly degenerate after the action ($T_e \ll T_{\text{F}}$, where T_{F} is the Fermi temperature). In these experiments, the ratio of the heat capacities $c_e/c_i \sim T_e/T_{\text{F}}$ and the thermal diffusivities χ_{1T}/χ_e were small down to 1/100. In the experiments performed in the 1990s, the back (with respect to the side facing laser action) boundary of a thin (d_f = 50–100 nm) film

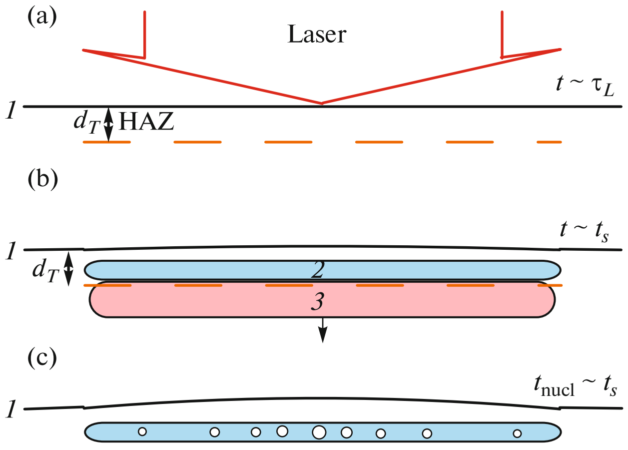

Fig. 1. (Color online) Early ($-\infty < t \le t_{\mathrm{eq}}$) and medium ($t \sim t_s$) stages. Three important points (from top to bottom). (a) Absorption of a laser pulse and the formation of HAZ of thickness d_T, (*1*) metal boundary. (b) Acoustic or medium stage $t \sim t_s$. An acoustic wave, which consists of compression segment *3* and tension segment *2* and goes to the target volume (arrow down), forms on the acoustic time scale. (c) Beginning of the first nucleation in segment *2*.

was rapidly heated (in several picoseconds). The $1T$ estimation of the heat propagation time gives

$$t \sim \frac{d_f^2}{\chi_{1T}} = 25\left(\frac{d_f}{50\ \mathrm{nm}}\right)^2\ \mathrm{ps}$$

at a usual value $\chi_{1T} \sim 1\ \mathrm{cm}^2/\mathrm{s}$. This difference in the heating times of films of the given thickness led to the term “ballistic” and suggested the two-temperature concept.

At the first stage, researchers restricted themselves to thermal analysis; at the second stage, they began to study the complete problem. In the complete problem, researchers cannot neglect the motion induced by an ultrashort laser action. In the complete formulation of the problem, the problem of creating surface nanostructures and nanoparticle generation can be resolved. Structures and particles appear when melting, tension, and the loss of continuity of condensed matter are taken into account along with the recrystallization and dynamics of solid, liquid, and vapor–gas media.

The transition to the second stage was initiated by works [11–13]. The authors of [11] observed Newton rings, the appearance and the accumulation of which in time could not be explained without dynamic concepts [12, 13]. As a result, the concepts of thermomechanical, or spallative, ablation during a femtosecond action appeared [12, 13]. Similar concepts of thermo- or photomechanical failure were independently formulated in the investigations of laser irradiation of polymers and biomaterials [14]. The motion of a medium becomes determining above the spallative ablation threshold, which depends on the type of substance. This threshold is about 50 mJ/cm^2 for absorbed energy F_{abs} (which is the threshold of bulk targets, the thicknesses of which exceed the thickness of the layer heated by an ultrashort pulse d_T [15]) for metals and the optical ultrashort action absorbed in a skin layer [15–17].

The main principles of spallative ablation are illustrated in Figs. 1 and 2. Time is calculated from the maximum of the laser pulse intensity at the boundary of metal 1. The width of arrow “laser” corresponds to the laser beam diameter on the absorbing surface. The $2T$ stage is characterized by the formation of heat-affected zone (HAZ) of thickness d_T at this stage (see Fig. 1). The time of the $2T$ stage is t_{eq}. As noted above (also see [10]), the heat-conducting ability of the electron subsystem increases due to the separation of the electron subsystem, which has a low heat capacity, from the ion subsystem with a high heat capacity (independence of Eqs. (1) and (2)). Thermal conductivity κ at the $2T$ stage (κ_{2T}) is much higher than at the $1T$ stage (κ_{1T}; see, e.g., [18, 19]). Therefore, layer d_T forms at an ultrasound velocity. Indeed, in the diffusion approximation [10], the HAZ thickness grows as $x \propto \sqrt{\chi_e t}$; then, we have

$$\frac{dx}{dt} \sim \sqrt{\frac{\chi_e}{t}} \sim \sqrt{\frac{l_e v_{\mathrm{F}}}{t}} \sim v_{\mathrm{F}}\sqrt{\frac{\tau}{t}},$$

where τ is the electron travel time. Fermi velocity v_{F} is much higher than velocity of sound $c_s \sim \sqrt{m_e/m_i}\,v_{\mathrm{F}}$. Therefore, many collisions are required for velocity dx/dt to decrease to the velocity of sound. This condition is operative at the $2T$ stage, when Eqs. (1) and (2) are split. The number of collisions in HAZ of thickness $x(t)$ is large; hence, the diffusion approximation is justified (non-Knudsen, i.e., nonballistic mode of heat propagation).

Figure 1a illustrates the formation of a layer of thickness d_T. As noted above, this is a supersonic process; after is completion, the HAZ layer expands and resolidifies due to heat removal to the metal volume at the rates that are well below the velocity of sound. Thus, layer d_T forms in time of the order of $d_T/(dx/dt)$ before the end of formation of the acoustic wave that goes into the metal volume (Fig. 1b, arrow down). The characteristic thickness and the wave formation time are d_T and $t_s = d_T/c_s$, respectively. Acoustic phenomena will be described in detail in the next section.

Figure 2 shows the situation at moderate late times at absorbed energy F_{abs}, which is higher than spallative ablation threshold F_{abl} by several times in the presence of environment $F_{\mathrm{abs|abl|wt}}$ (let water be the environment for definiteness). Note that threshold $F_{\mathrm{abs|abl|wt}}$ is significantly higher than the threshold of ablation into vacuum $F_{abs|\mathrm{abl|vac}}$, which will be discussed in the next section. The times that exceed scale t_s by several times are called moderate late times. Curve *1* in Fig. 2 outlines the metal boundary. The foam in Fig. 2a forms from the nucleation bubbles shown in Fig. 1c.

At $F_{\rm abs} \approx F_{\rm abs|abl|vac}$, the bubble layer is thin ("single" nucleation) and foam is almost absent. When threshold $F_{\rm abs|abl|vac}$ is exceeded severalfold, sequential multiple nucleation takes place. Leaping ahead, we note that the presence/absence of a transparent weakly heat-conducting liquid at the contact with a target does not affect nucleation. After the first nucleation, the tensile stress in the nucleation layer becomes very low (see Fig. 1c). A spallation pulse, which releases the tensile stress, begins to move behind the acoustic wave from the nucleation layer. However, the tensile stress (behind a compression wave with a sufficiently high amplitude) again begins to grow in absolute value after the first nucleation. As a result, the second nucleation occurs in the layer that is farther from the contact boundary (CB) than the first nucleation layer. The number of nucleation events is determined by overcoming threshold $F_{\rm abs|abl|wt}$. A thick foam layer forms during multiple nucleation (see Fig. 2a).

The foaming of metals, semiconductors, and polymers by an ultrashort laser action was considered beginning from works [13, 14] (also see [20–32]). The mechanical characteristics of foam (tension resistance, cellular structure) were analyzed in [22, 27, 32]. A finite laser beam size was taken into account in [31]. The authors of [25] were the first to assume that the freezing of a foamed substance causes the formation of chaotic surface nanostructures observed in experiments.

Plasmons are excited in illuminated nanostructures. Plasmon dissipation leads to a sharp decrease in the reflection coefficient of a nanostructured surface (blackening) as compared to an ideal flat surface made of the same metal.

The problems of the solidification of a melt in foam were studied in [21, 23, 24, 28, 30–32]. The final frozen nanostructures (i.e., those observed in a long time after the end of all processes) on an irradiated surface were experimentally analyzed in [33, 34]. The authors of these works studied foaming during expansion into vacuum. In this work, we investigate the formation of extensive foam and the subsequent evolution in the presence of material environment, which retards the expansion of a foamed substance.

Curve I in Fig. 2 separates the foam into two parts. The upper part sticks gradually onto CB (Fig. 2, curve *1*) and the lower part is still related to the crater bottom and the retained bulk target. The solidification of the lower part results in the formation of nanostructures on the crater surface. Below curve II in Fig. 2, the foam made of Voronoi cells has time to decompose into a vapor–liquid mixture consisting of droplets [29]. A cellular structure forms gradually from vapor–liquid mixture bubbles as the volume fraction of the liquid phase in the mixture decreases. The foam between curves II and *5* in Fig. 2 has no time to decompose into droplets before it precipitates onto boundary *5* of layer *4* of a continuous metal. Droplets from the region between curves I and II in Fig. 2 then precipitate onto this layer. The precipitation of foam and droplets onto layer *4* is related to the deceleration of layer *4*, which is caused by the action of the liquid from the outside. Layer *4* is decelerated, whereas the droplets in foam fly under their own inertia, since the foam outside layer *4* does not know about the existence of an external stopping medium. The foam begins to slow down only when it penetrates into layer *4*. Note that pressure $p_{\rm I-5}$ in the foam is determined by the evaporation of the liquid metal.

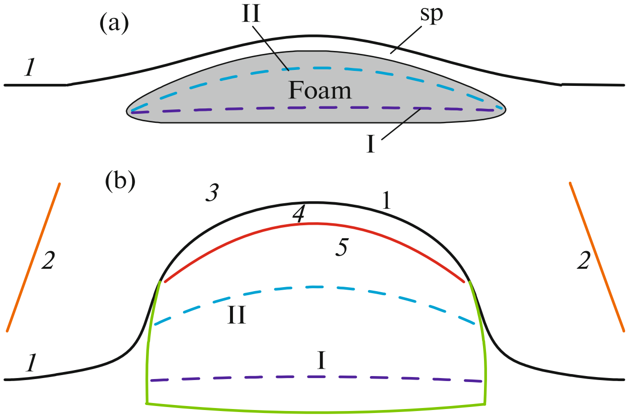

Fig. 2. (Color online) Late stages, when foam forms from cavitation bubbles in Fig. 1c. The volume fraction of liquid in the vapor–liquid mixture decreases in time and foam is broken along line I: (a) expansion into vacuum (weakly qualitatively differs from the case of expansion into condensed matter) and (b) expansion into a medium with a low (as compared to metal impedance $Z_{\rm Au}$) but finite acoustic impedance $Z_{\rm wt}$. (*1*) CB, (*2*) SW in stopping medium, (*3*) stopping medium near CB, (*4*) continuous metal layer, and (*5*) boundary between layer *4* and foam. SP is spallation plate.

In layer *4* at the moderate late stage, the pressure drops from pressure p_{CB} at CB to pressure $p_{\rm I-5}$ (see Fig. 2). The situation depends on absorbed fluence $F_{\rm abs}$. Here, we restrict ourselves to the case where a pulse is ultrashort and $F_{\rm abs}$ slightly (severalfold)) exceeds the nucleation threshold in the presence of an external medium ($F_{\rm abs|abl|wt}$). When threshold $F_{\rm abs|abl|wt}$ is slightly overcome, the continuous metal layer at CB is a spallation plate, or a spallation shell in the case of a finite laser beam diameter (see Fig. 1a). When the excess over the threshold increases, the spallation plate becomes thinner, and it disappears at "evaporation" threshold $F_{\rm ev}$ [27, 35]. These considerations for $F_{\rm ev}$ are related to the case of ablation into vacuum.

In the case of vacuum, a vapor layer is located above the boundary of the spallation shell in the fluence range $F_{\rm abs|abl|vac} < F_{\rm abs} < F_{\rm abs|ev}$. This layer is formed due to evaporation from the boundary of the spallation

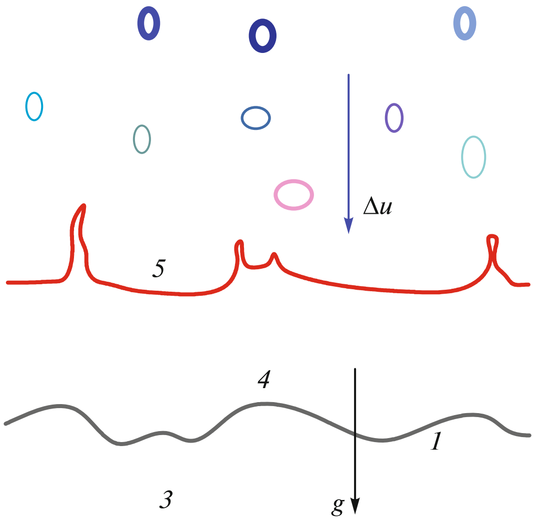

Fig. 3. (Color online) Atmosphere *4* in gravitational field (free fall acceleration g) supported by water *3*. The coordinate system is related to CB. The digital designations are identical to those in Fig. 2: (*1*) gold–water contact and (*5*) upper atmosphere boundary. Two-phase medium *5*–II–I streams and droplets fall on this atmosphere at velocity Δu (see Fig. 2).

shell. The vapor layer mass can be estimated using the Hertz–Knudsen formula and the saturated vapor density taken from the ion temperature [27, 36, 37]. The influence of the electron temperature on the evaporation energy is unknown (this effect is only substantial in the short $2T$ stage). This vapor mass estimation gives about one nanometer (3–4 monoatomic layers) near threshold $F_{\rm abs|abl|vac}$. The evaporated layer near this threshold is geometrically thin, since the velocity of sound in vapor is low. This behavior is seen from the density profiles in [27, 36]. In comparison with the foam thickness, the evaporated layer remains thin even at fluences $F_{\rm abs} \approx F_{\rm abs|ev}$, where the intersection of an unloading adiabat with a binodal approaches the critical point in a boiling curve [27, 36]. Although the substance of the vapor layer belongs to the two-phase region, no signs of vapor condensation into droplet nucleation centers were detected at the molecular dynamics simulation times [27, 36]. These times are on the order of several sound scales t_s. The vapor layer without condensation exists in front of the two-phase region and slightly above threshold $F_{\rm abs|ev}$ (see Figs. 12, 14, 15 in [27]).

Threshold $F_{\rm abs|ev}$ is likely to disappear in the case of ablation into a stopping medium. A spallation plate and a cavity under it appear above threshold $F_{\rm abs|abl|wt}$. As energy $F_{\rm abs}$ grows over threshold $F_{\rm abs|abl|wt}$, the plate becomes thinner, the cavity becomes thicker, and the substance mass in foam increases (see Fig. 2a). When $F_{\rm abs}$ increases, the spallation plate does not disappear: the CB retardation “rakes” the metal to CB. The metal transforms into a continuum until pressure p_{CB} is higher than vapor pressure $p_{\rm I-5}$ at boundary *5* in Fig. 2b. The condition $p_{CB} > p_{\rm I-5}$ is necessary for both Figs. 2a and 2b, otherwise no deceleration takes place. Therefore, from a fundamental standpoint, both metal layers at CB in Figs. 2a and 2b seem to be sufficiently equivalent. However, on the other hand, the spallation plate in Fig. 2a is retained when the environment density vanishes, and the layer in Fig. 2b disappears in this case.

CB retardation g in the coordinate system related to CB is equivalent to the effective gravitational field with free fall acceleration g. The height of a uniform gold atmosphere in this gravitational field is estimated (using ideal gas formula) at

$$h_{\rm atm}[{\rm nm}] = \frac{k_{\rm B}T}{m_i g} = 40\frac{T_{\rm kK}}{g_{14}}, \tag{4}$$

where $T_{\rm kK}$ is the metal temperature near CB in kilokelvins and $g = 10^{14}g_{14}$ cm/s^2. The maximum possible pressure at CB is estimated by the ideal gas formula,

$$p_{CB}^{\max}[{\rm GPa}] = nk_{\rm B}T = 0.83(\rho/\rho_0)T_{\rm kK},$$

were $\rho_0 = 19.3$ g/cm^3 is the gold density under normal conditions. The lower pressure p_{CB} at CB as compared to $p_{CB}^{\max}$, the more condensed state of the metal.

From here on, we will consider the water–gold pair. Atmosphere or the spallation layer is supported by the underlying shock-compressed water (if the pictures in Fig. 2 are turned over as is shown in Fig. 3). Atmosphere is in quasi-hydrostatic equilibrium, since it is a condensed phase with a high velocity of sound (in contrast to the two-phase medium). Sound passes through atmosphere in the vertical direction faster than deceleration $g(t)$ changes. The velocity of sound in two-phase region 5–II–I in Fig. 2 (region above curve *5* in Fig. 3) is very low. The liquid in this region flies under its own inertia and effective deceleration g does not affect it. As a result, excess velocity ΔV shown in Fig. 3 appears. The precipitation of substance (foam or droplets) 5–II–I from Fig. 2 onto layer *4* in Figs. 2 and 3 is similar to accretion of gas onto the atmoshpere in astrophysics [38–42]. However, in contrast to astrophysics, the accretion substance is in the two-phase state (liquid–vapor). After foam precipitation the vapor spaces in the two-phase medium close, and the precipitated matter becomes a single-phase substance in the atmosphere or the spallation layer.

Astrophysics considers the accretion of a neutron star surrounded by a magnetosphere [38, 39; 41, section 8.3; 42, section 5]. First, an accretion flux in the state of free fall on the star exists instead of region 5–II–I in Fig. 2. Second, a hydrostatic atmosphere, which is analogous to layer *4*, intercepts the accretion flux. The atmosphere consists of diamagnetic plasma rejecting a magnetic field. The atmosphere (hydrostatic shell of magnetosphere) rests on the star magnetosphere. Third, the magnetic field supporting the atmosphere is analogous to the low-density substance in region *3* in Figs. 2 and 3. The contact between plasma and magnetic field in the gravitational field of the star (CB 1 in our case) is unstable with respect to the development of a magnetic analog of the Rayleigh–Taylor instability.

A similar situation with the atmosphere that forms due to the interstellar medium drag appears during the expansion of supernova remnant [41–43]. Another example is the expansion of the products of detonation of a condensed explosive into the ambient gas [44, 45]. In both cases, deceleration by an external substance and the feed of the atmosphere–shell by an internal flux take place, and the internal flux is supersonic. Therefore, the following two shock waves appear: an external shock wave in the stopping medium and an internal shock wave at the internal boundary of the atmosphere.

Accretion is related to mass increment $\dot{m}$ [g s^{-1} cm^{-2}] and momentum increment $\dot{m}\Delta u$ into layer *4* in Figs. 2 and 3. The mass increment gradually increases the geometric thickness of the atmosphere and is one of the causes of decreasing the rate of deceleration g. The addition of momentum is equivalent to the pressure applied to layer *4* from boundary *5* in Figs. 2 and 3. This addition also increases the stopping time of the spallation plate. Soon after flux $\dot{m}$ is exhausted, the plate stops.

Pressure p_{CB} at the contact consists of the following three components: first, the atmosphere weight $g\int_1^5 \rho dx$ (limits 1 and 5 mean layer *4* boundaries in Figs. 2, 3); second, momentum flux $\dot{m}\Delta V$; and third, vapor pressure from two-phase region 5–II–I (see Fig. 2). Figure 4 shows the saturated gold vapor pressure according to the wide-range equation of state of gold [46–48]. For comparison, Fig. 4 also presents six points from Wikipedia [49] and the boiling point of gold [49]. It is seen that the last point from [49] at a pressure 1 bar = 100000 Pa and the boiling point at a pressure 1 atm = 101325 Pa have slightly different temperatures.

As is seen from Fig. 3, contact *1* is unstable with respect to the Rayleigh–Taylor instability (RTI), since the effective weight is directed from heavy gold (layer *4*) to light water (space *3*) [39, 41, 42, 50, 51]. However, the conditions are far from standard ones (stationary state, incompressible liquid, infinite layer thickness). Of course, to make a conclusion regarding the role of RTI, we have to comprehensively study the one-dimensional flow against the background of which perturbations grow. This is the aim of the next section.

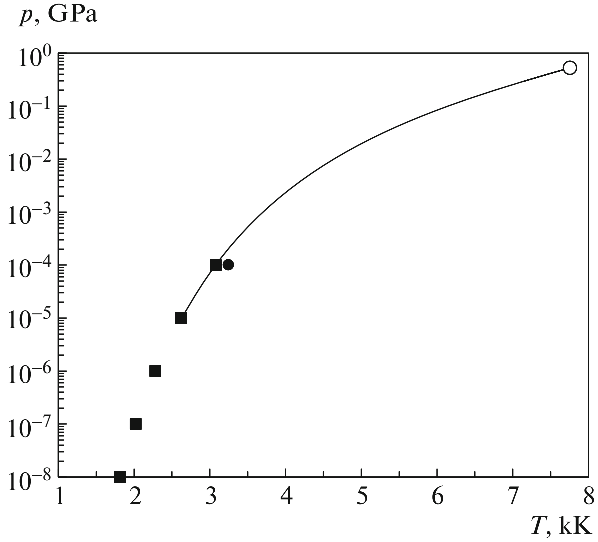

Fig. 4. (solid line) Saturated gold vapor pressure according to the wide-range equation of state [46–48]. This curve is roughly approximated by the formula $p_{\rm sat}$ [GPa] = 35exp(−39.95/T [kK] + T [kK]/9): (■) experimental points. Critical point (○) has the coordinates $T_{\rm cr} = 7.8$ kK, $p_{\rm cr} = 0.53$ GPa, and $\rho_{\rm cr} = 5.3$ g/cm^3; ● experimental saturate vapor pressures.

2. GENERAL PICTURE

Our analysis of the situation is based on numerical simulation. It is important to begin with the discussion of the general picture for the rather complex details revealed by simulation to be clear. We now consider the post-2T stage, which begins after the equalization of the electron (T_e) and ion (T_i) temperatures. The point is that the 2T stage is short and heat propagation in it is supersonic. Therefore, to a first approximation, we may neglect the time of the 2T stage ($t_{\rm eq}$). Here, we analyze acoustic phenomena at acoustic times $t_s = d_T/c_s$; that is, a high-pressure layer of thickness d_T is formed by fast heat conduction during the time interval $t_{\rm eq} > \tau_L$. The pressure wave leaves the layer d_T during the acoustic stage lasting t_s. This approximation (with small parameter $t_{\rm eq}/t_s$) is worse for gold, where time $t_{\rm eq}$ is rather long (5–7 ps). For other metals, we have $t_{\rm eq} \sim 1$ ps. In the case of gold, the heating thickness is large, $d_T \sim 150$ nm. Therefore, the acoustic scale t_s is 50 ps; we have $c_s \approx 3$ km/s = 3 nm/ps.

As the initial data at the post-2T stage, we have an instantly created heating layer of thickness of thickness d_T, the layer substance is at rest, and the thin substance layer at the periphery is neglected. (The thickness of this thin layer is $c_s t_{\rm eq}$ and it is involved in motion by the 2T rarefaction wave.) Let we have $d_T = \infty$ from the very beginning. Then, the "compression" region (high-pressure region created by instantaneous heating) is infinite and the rarefaction wave is self-similar. This situation was studied in [52–56].

When comparing the rarefaction waves in a gas and a condensed medium (solids, liquids), we note that the

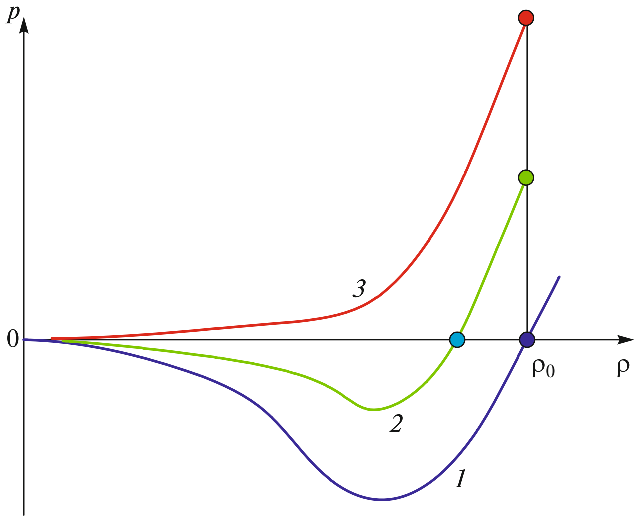

Fig. 5. (Color online) Expansion adiabats or isotherms corresponding to increasing entropy $s_1 < s_2 < s_3$ or temperature $T_1 < T_2 < T_3$. Digits number curves. Regions $p < 0$ from the point of intersection of axis $p = 0$ to the minimum belong to metastable states.

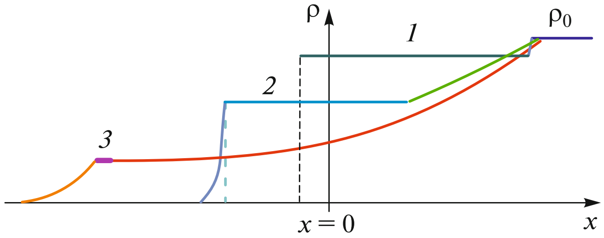

Fig. 6. (Color online) Rarefaction wave profiles in the model with instantaneous heating ($t_{eq}/t_s \ll 1$) and a large heating depth ($d_T = \infty$). Numerals *1–3* belong to curves *1–3*, respectively, in Fig. 5 with increasing values of F_{abs}. Profiles consist of four segments (see text).

cohesion of the condensed phase most strongly affects the shape of a rarefaction wave. “Zero” pressure appears in the adiabats and isotherms of condensed matter because of interatomic attraction, and zero pressure is reached at a finite density (see below; we will explain why zero is put in quotes). Figure 5 shows adiabats and isotherms. The gas adiabats and isotherms qualitatively resemble curve *3* in Fig. 5. The pressure on them is determined by the kinetic energy of atomic motion and is positive elsewhere.

It is important that pressure $p(\rho)$ in Fig. 5 vanishes at a finite substance density ρ_{eq} because of atomic cohesion in condensed states. This density is called equilibrium density, and the $\rho_{eq}(T)$ dependence determines the thermal expansion of condensed matter related to anharmonic terms. Densities $\rho_{eq}(T > 0)$ are lower but comparable with solid-state density $\rho_{eq}(0)$. The condition $\rho_{eq}(T) = 0$ plays a key role in the expansion hydrodynamics in a laser rarefaction wave. Indeed, the vacuum (medium into which expansion takes place) pressure is zero. Thus, the curve segment from initial point ρ_0, $p(T)$ (green circle) to the point of intersection with axis $p = 0$ (blue circle $\rho = \rho_{eq}$, $p = 0$) in Fig. 5 describes the self-similar rarefaction wave during the expansion of an instantaneously heated substance into vacuum [53–56]. The dependence on x, t is reduced to the dependence on self-similar variable x/t, where x is measured from the initial position of CB and t is measured from the beginning of instantaneous heating [53–56].

At point ρ_{eq}, $p = 0$ (blue circle in Fig. 5), the dynamic boundary condition that conjugates a substance to vacuum is met. “Instantaneous” heating (approximation $t_{eq}/t_s \ll 1$) throws a substance from point ρ_0, $p = 0$, which belongs to the state before an ultrashort action, to state ρ_0, $p(T(F_{abs}))$ in the initial density ρ_0 isochore in Fig. 5. The higher absorbed energy F_{abs}, the higher the initial point (initial state) from which a rarefaction wave starts in the ρ_0 isochore.

The four segments that make up the profiles in Fig. 6 are as follows.

First, it is the initial state with the same density ρ_0 and different initial pressures *1*, *2*, and *3*. These pressures are given in Fig. 5. Profile *1* in Fig. 5 starts from axis $p = 0$. The initial pressure in Fig. 5 should be slightly lifted above zero to obtain density profile *1* in Fig. 6. Profile *1* in Fig. 6 is described in the linear acoustic approximation at a high accuracy, since the pressures are low as compared to the bulk modulus of the condensed matter, the velocities are low as compared to the velocity of sound, and the decrease in density decrement $\delta\rho$ in the rarefaction wave is small as compared to ρ_0. The profiles of type *1* correspond to the rapidly heated states of a solid body or a melt slightly above the melting curve. The substance is assumed to be at rest under room conditions before the action.

Second, it is a centered rarefaction wave with a fan of characteristics [53–56]. The fan in Fig. 6 includes the density decrease between the first and second uniform-flow regions. Numerals *1*, *2*, and *3* are over the second uniform region in Fig. 6. This region is called a step, or a plateau, and it corresponds to the point of intersection with axis $p = 0$ in the phase plane (ρ, p) in Fig. 5.

Third, it is the plateau in Fig. 6.

Fourth, it is the vapor “tail” connecting the plateau with vacuum. The tail corresponds to a fan of other characteristics, at which the velocity of expansion of a flux into vacuum is higher than in the fan in the second segment. If the Riemann method and equilibrium adiabats and isotherms are used to solve the gas dynamics equations, the tail passes only through the two-phase region under the binodal in the (ρ, T) plane in the case of adiabat and passes partly through the two-phase region and partly through the single-phase gas region in the case of isotherm. The corresponding adiabats and isotherms are shown in Fig. 7. In a vapor layer (adiabat) or a vapor–gas layer (isotherm), the pressure decreases from saturated vapor pressure $p_{\text{sat}}(T)$ to zero vacuum pressure (see Fig. 7). Note that no condensate formation is detected in the vapor part of the tail in the molecular dynamics simulations given below on our space–time scales.

Binodal *b* in Fig. 7 bounds the region of equilibrium two-phase states. When the substance in an equilibrium rarefaction wave expands to the binodal, the pressure decreases to saturated vapor pressure $p_{\text{sat}}(T)$ (see Figs. 5, 7). The values of $p_{\text{sat}}(T) < p_{\text{cr}}$ are small as compared to initial pressures $p_0(\rho_0) > 7$ GPa for the heating under study above ablation threshold $F_{\text{abs|abl}}$ (see Fig. 4). The critical pressure is $p_{\text{cr}} = 0.53$ GPa according to the equation of state of gold [46–48]. The kink point in the equilibrium profile in Fig. 5 is located slightly above axis $p = 0$, at pressure $p_{\text{sat}}(T)$, rather than in this axis. Since $p_{\text{sat}}(T) \ll p_0(F_{\text{abs}})$, the kink point in Fig. 5 is paced in axis $p = 0$. In all other features, Figs. 5 and 7 are identical.

It is seen that, as F_{abs} increases (curves $1 \to 2 \to 3$), the negative pressure well in Fig. 5 becomes shallower and the spatial profile of the rarefaction wave shown in Fig. 6 (profiles $1 \to 2 \to 3$) deforms simultaneously. As noted above, the cases with relatively weak heating (curve and profile *1*) are described in the linear acoustic approximation. Here, the velocity of metal expansion in the plateau is

$$u = \frac{p_0(F_{\text{abs}})}{Z_A} = \frac{p_0(F_{\text{abs}})}{B} c_s,$$

where $Z_A = \rho c_s$ is the acoustic impedance of gold and B is the bulk modulus. Correspondingly, the left edge of the plateau in Fig. 6 travels distance ut from $x = 0$ at time t measured from the maximum of the laser pulse. The head characteristic of the fan of characteristics is located at distance $c_s t$ in Fig. 6. This characteristic in Fig. 6 moves to the right, to the substance volume.

As F_{abs} increases, the pressure drop amplitude in the expansion segment from the initial density to the plateau density increases, the plateau density decreases, the substance velocity in the plateau increases, and the plateau length decreases (cf. plateaus under numerals *1*, *2*, and *3* in Fig. 6). In addition, the tail length increases. The plateau becomes small and disappears at high values of F_{abs}, when the intersection with the binodal approaches the critical point. The profile of the rarefaction wave resembles its profile in the case of gas.

Here, we have dwelt on the solutions at $t_{\text{eq}} \ll t_s$ and $d_T \gg c_s t_{\text{eq}}$, since we need a qualitative understanding before passing to numerical results. Figures 5–7, which were plotted for expansion into vacuum, will help us to describe the situation during expansion into an material environment. On a fundamental level, these two cases are different because of the dynamic boundary condition $p_{CB} = 0$ (vacuum) against $p_{CB} > 0$ (stopping environment); that is, we will simply increase the external pressure from $p_{CB} = 0$ to $p_{CB} > 0$. Self-similarity is retained if the external pressure is constant in time and the instantaneously heated layer thickness is infinite.

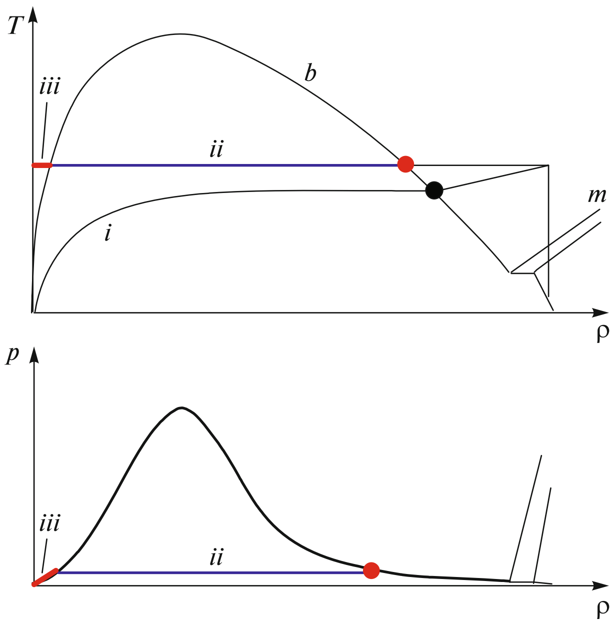

Fig. 7. (Color online) Phase diagrams in planes (ρ, *T*) and (ρ, *p*). Comparison of the shapes of (*i*) adiabatic and (*ii*) isothermal profile tails from Fig. 6. *b* stands for binodal; *m*, for melting region. Vertical temperature or pressure jump ρ_0 corresponds to the rapid heating approximation $t_{\text{eq}} \ll t_s$.

Let T_{bin} be the temperature at the point of intersection of an adiabat and a binodal at given F_{abs}. We assume that the instantaneously heated substance in the rarefaction wave expands with retained entropy and that the binodal is the curve of coexistence of the vapor and condensed phases. The following two modes are possible.

In mode 1, external pressure p_{CB} (which is taken to be constant in time) is lower than saturated vapor pressure $p_{\text{sat}}(T_{\text{bin}})$, and the pressure in the plateau is $p_{\text{sat}}(T_{\text{bin}})$. A uniform flow layer is adjacent to the contact, where pressure p_{CB} is constant. The right edge of this layer has the characteristic of the second fan of characteristics, i.e., the tail (see Fig. 6). Then, the remaining part of the two-phase tail, where the pressure increases to the right (i.e., toward the target volume), is present. This increase begins with p_{CB} and continues to the point where the tail joins the plateau with pressure $p_{\text{sat}}(T_{\text{bin}})$. Plateau $p_{\text{sat}}(T_{\text{bin}})$ then exists to the right. The first fan of characteristics, which connects plateau $p_{\text{sat}}(T_{\text{bin}})$ and the head characteristic that runs on the unperturbed instantaneously heated substance, is located farther to the right. As noted above, the adiabat segment between the green and blue points in Fig. 5 corresponds to the first fan in the phase thermodynamic plane. The heat characteristic corresponds to the green point and the plateau with pressure $p_{\rm sat}(T_{\rm bin})$ corresponds to the blue point. Thus, the following two plateaus occur in the first mode: the plateau at pressure p_{CB} and the plateau at pressure $p_{\rm sat}(T_{\rm bin})$.

In mode 2, external pressure p_{CB} is higher than saturated vapor pressure $p_{\rm sat}(T)$. Then, a uniform flow layer (plateau) is adjacent to CB with external pressure p_{CB} region. The internal characteristic of the first fan becomes the right boundary of this plateau, which means that the expansion adiabat in Figs. 5 and 7 does not reach the binodal.

It is this situation that takes place in a long initial time interval in the interaction between gold and water under study. Therefore, from here on we consider mode 2. Of course, in real situation with finite depth d_T of a heated layer, pressure $p_{CB}(t)$ at CB decreases strongly during long-term expansion into water. Contact temperature $T_{CB}(t)$ on the side of gold remains unchanged, and saturated vapor pressure $p_{\rm sat}(T_{CB})$ eventually exceeds $p_{CB}(t)$. First, this situation takes time; second, this situation does not occur if gold temperature $T_{CB}(t)$ decreases sufficiently rapidly, so that pressure $p_{\rm sat}(T_{CB}(t))$ decreases faster than $p_{CB}(T)$. These problems will be considered after analyzing numerical calculations.

The main point is that the uniform flow region near CB on the side of metal is retained in mode 2. This is again plateau, and the plateau pressure is determined by external pressure p_{CB}, $p_{CB} > p_{\rm sat}(T_{\rm bin})$, rather than being $p_{\rm sat}(T_{\rm bin})$.

Plateau height $p_{\rm sat}(T_{\rm bin})$ is low as compared to the pressure in the isochore for expansion into vacuum at the high values of absorbed energy $F_{\rm abs}$ under study,

$$p_{\rm sat}(T_{\rm bin}) \ll p_0(F_{\rm abs}) \sim 100\ {\rm GPa},$$

$$p_{\rm sat}(T_{\rm bin}) \le p_{\rm cr} = 0.53\ {\rm GPa},$$

where $p_0(F_{\rm abs})$ is the pressure in the isochore $\rho = \rho_0$ after instantaneous heating (see Figs. 5, 7). On the other hand, the Hugoniot adiabats of water are such that pressure p_{CB} at the gold–water CB is rather high at the initial stage at the given values of $F_{\rm abs}$ (see discussion below). This pressure is higher than the critical gold pressure by an order of magnitude, $p_{CB} \gg p_{\rm cr}^{\rm Au}$. In this case, the contact pressure is low as compared to the pressure in the initial density isochore immediately after heating, $p_{CB} \ll p_0(F_{\rm abs})$. Thus, we have $p_{\rm cr}^{\rm Au} \ll p_{CB} \ll p_0(F_{\rm abs})$ in our situation at the initial stage. This profile belongs to mode 2.

We analyze the cases at $F_{\rm abs}$ such that a plateau is weakly pronounced during expansion into vacuum, the point of intersection of adiabat and binodal in Fig. 7 is to the right or to the left of the critical point, and the profile resembles gas expansion. However, a near-contact plateau appears because of the counteraction of water (mode 2), and such a plateau also appears in the case of gas during the decay of pressure discontinuity. Let us explain the decay of discontinuity or jump in gas dynamics. At $t < 0$, we have two homogeneous half-spaces that are in contact through a rigid wall. The right half-space has a high density and a high pressure (gold), and the left half-space has a low density and pressure (water). At $t = 0$, the wall is simultaneously removed. As a result, a flow with a rarefaction wave in gold, a near-contact plateau, and a shock wave in water appears.

Obviously, the gold region affected by the difference between water and vacuum is bounded by the plateau layer. Outside this layer, the expansion of gold is identical to the case of vacuum.

We now estimate contact pressure p_{CB} and velocity u_{CB} in terms of linear acoustics in both water and gold. We put the pressure and the velocity in water equal to the plateau pressure and velocity and obtain

$$p_{CB} = \frac{\xi p}{1+\xi}, \quad u_{CB} = \frac{p_{CB}}{Z_{\rm wt}}, \tag{5}$$

where $\xi = Z_{\rm wt}/Z_A \approx 0.03$, $Z = \rho c_s$ is the acoustic impedance, $Z_{\rm Au}$ is the impedance of gold, $Z_{\rm wt}$ is the impedance of water, and p is the pressure in gold outside the rarefaction-wave-affected zone. At p = 100 GPa, we have

$$p_{CB} = 3\ {\rm GPa}, \quad u_{CB} = 1.8\ {\rm km/s}. \tag{6}$$

Another estimate follows from the Hugoniot adiabat of water [57],

$$D = c + 1.8u_{CB}, \tag{7}$$

where D is the shock wave (SW) velocity in water and c = 1.6 km/s is the velocity of sound in water under normal conditions. Shock-compressed water is more “rigid” than that in linear acoustics. Therefore, the pressure at CB turns out to be higher than that calculated by Eq. (5) and the contact velocity is lower. We search for p_{CB} and u_{CB} in the case where gold is described in the linear acoustics approximation and water is described by Hugoniot adiabat (7). Indeed, the bulk modulus of water ($B_{\rm wt} = \rho_{\rm wt}^0 c^2$) is comparable with the pressure estimated by Eq. (5) at $p \sim 1$ Mbar ($\rho_{\rm wt}^0$ is the water density under normal conditions). Therefore, the nonlinear effects that occur in water during the decay of discontinuity are substantial. We write

$$u_{CB} = (p - p_{CB})/Z_{\rm Au}, \tag{8}$$

$$\frac{V}{V_0} = 1 - \frac{u_{CB}}{c + 1.8u_{CB}}, \tag{9}$$

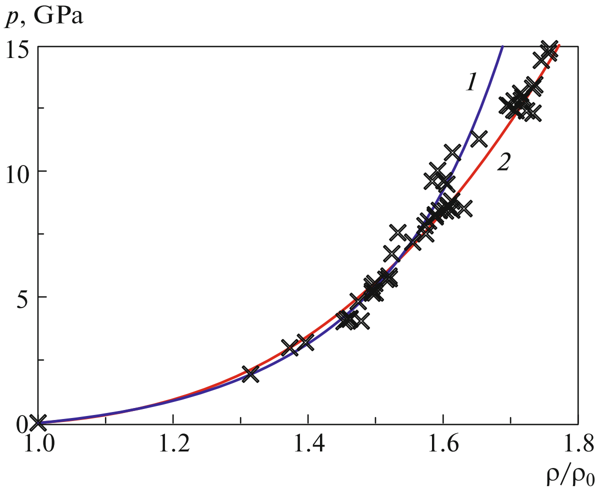

Fig. 8. (Color online) Hugoniot adiabat in the moderate compression region: (symbols) data of various experiment series taken from [48]; (*1*) calculation by Eq. (10); and (*2*) approximation dependence (12), which is valid in the pressure range from 0 to approximately 1 Mbar (see Fig. 9).

$$p_{CB} = B_{\mathrm{wt}} \frac{1 - V/V_0}{[1 - 1.8(1 - V/V_0)]^2}, \tag{10}$$

where p is the still the pressure in gold outside the rarefaction-wave-affected zone and V/V_0 is the degree of water compression in SW. Equation (8) gives the gold velocity during acceleration from an immobile state under pressure drop from p to p_{CB}. Equation (9) follows from the SW kinematics and the mass conservation condition. Equation (10) represents the law of conservation of momentum in SW (pressure in front of SW is neglected). Solving this system at p = 100 GPa, we find

$$p_{CB} = 6.9 \text{ GPa}, \quad u_{CB} = 1.6 \text{ km/s}. \tag{11}$$

Pressure p_{CB} (Eq. (11)) is seen to change twofold as compared to pressure (6), whereas velocity $u_{CB} \approx p/Z_A$ decreases insignificantly (provided $p \gg p_{CB}$). The condition $p \gg p_{CB}$ means that near-contact phenomena occur at the foot of the high pressure "hill" (Fig. 6, curve *3*). Thus, the CB velocity (u_{CB}) is mainly generated in relieving high pressure p along the first fan of characteristics of the rarefaction wave in heated gold.

Figures 8 and 9 show the Hugoniot adiabats of water plotted using the experimental data collected in [48]. These data are approximated by the relationship

$$\begin{gathered} p = 2.25x + 7.07x^2 + 25.08x^3 - 7.04x^4, \\ x = \rho/\rho_0 - 1, \end{gathered} \tag{12}$$

which is shown in Figs. 8 and 9. Pressure p in Eq. (12) is given in GPa. Approximation (12) provides a velocity of sound of 1.5 km/s for small compression and is valid at a pressure of about 100 GPa.

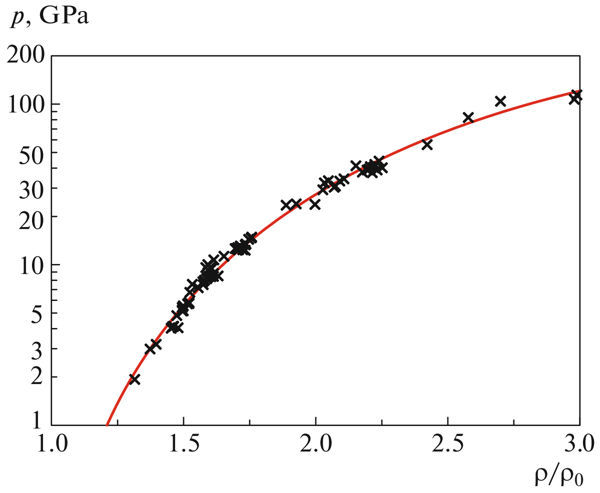

Fig. 9. (Color online) (symbols) Hugoniot adiabat of water according to the available data [48]. (line) Approximation (12) of these data.

Equation (12) is used to describe water during two-temperature one-dimensional numerical hydrodynamic simulation (2*T*HD code). In the 2*T*HD calculations, we neglect the heat-conduction heating of water, since the thermal conductivity of water related to molecule vibrations is low as compared to the thermal conductivity of gold. This effect is taken into account in molecular dynamics simulations. The irreversible heating of water associated with dissipation in SW is weak at pressures (6) and (11). In the 2*T*HD calculations, we apply Eq. (12) as the Hugoniot adiabat of water instead of the equation of state of water and take into account the shock-compression-induced reversible part of heating.

Gold is assumed to obey linear acoustics in estimate (5) and Eqs. (8)–(10). Indeed, the bulk modulus of gold (1.8 Mbar) is high even in comparison with the pressure considered above (p ~ 1 Mbar). However, the increase in the pressure during laser irradiation is related to heating. The linearization of the gas dynamics equations in small perturbations leads to acoustic and entropy modes (entropy–vortex mode in a multidimensional case). Acoustic modes run away from an initiation layer at the velocity of sound, and the entropy perturbation remains "frozen" in a substance; that is, a hot surface layer is retained in the cooling time due to heat conduction. It is this hot layer that is the arena of the active hydrodynamic phenomena (foaming, internal evaporation) to be studied below. The nucleation of cavities with a vapor phase and foaming appear when a finite heating layer thickness d_T is taken into account. No nucleation takes place under the conditions considered above, where $d_T = \infty$.

The condition of linearity (i.e., smallness) of an entropy perturbation in condensed matter means that the change from room temperature to a final temperature is small as compared to the critical temperature. Then, the decrease in the density $\delta\rho$ during thermal expansion is small as compared to gold density ρ_0 under normal conditions. However, this condition is not met in the situations under study: overheating to the temperatures comparable with the critical temperature and high-amplitude gold expansion with $\delta\rho \sim \rho_0$ take place. A nonlinear hot layer (nonlinear entropy perturbation) of thickness $d_T \sim 150$ nm appears. An analysis of this situation needs a numerical simulation. It is interesting that the compression wave goes into the volume from layer d_T having generated it and becomes quasi-linear, since the compression pressures in this wave are comparable (slightly lower than) with the bulk modulus at the values of F_{abs} under study.

3. TAKING INTO ACCOUNT A FINITE HEATING DEPTH

In Section 2, we considered the case called the decay of discontinuity in textbooks on the mechanics of fluids. At time $t = 0$, the wall between two homogeneous half-spaces (in our case, gold/vacuum or gold/water) having different pressures is removed. The flow at $t > 0$ is self-similar. In our case, a rarefaction wave runs in gold, which is under high pressure, at the velocity of sound, and SW moves into water.

In Section 2, the heating layer thickness is $d_T = \infty$; therefore, the half-space occupied by gold is homogeneous (ρ, p, and T distributions are uniform at $t < 0$). If thickness d_T is limited (in our case, $d_T \approx 150$ nm), a self-similar solution exists for $t \ll t_s$ and $t_s = d_T/c_s$. At times $t \sim t_s$, self-similarity ceases to be valid, and the motion mode called the decay of an “instantaneously” heated hot layer of finite thickness at CB with vacuum or water begins to be operative.

In acoustic terms, the flow at $0 < t \le t_s$ is represented as the sum of four acoustic (i, ii, iii, iv) and one entropy mode. The entropy mode and three acoustic modes (i, ii, iii) are in gold. Two acoustic modes (i, ii) run from the hot layer inside gold. The first of them is compression wave CW$^+$ (i); superscript “+” means that the wave propagates along axis x, which is directed into the gold volume, as in Fig. 6. Wave CW$^+$ (i) propagates to the right, into the gold volume. Another compression wave CW$^-$ (ii) runs to the left, to CB. Wave CW$^-$ (ii) is reflected from CB in the form of a rarefaction wave in gold, RF$^+$ (iii), and moves into water in the form of SW in water SW (iv). The existence of wave CW$^-$ (ii) is bounded by time interval t_s. After this time interval, wave CW$^-$ (ii) is fully transformed: (ii) $\rightarrow$ (iii) and (ii) $\rightarrow$ (iv). Waves (i), (iii), and (iv) live for an infinite time.

At $d_T = \infty$, pressure p in the first (head) characteristic of wave RF$^+$ (iii) remains constant, equal to p_0 in the uniform gold thickness. At finite d_T, pressure p in this characteristic decreases in time t_s. This pressure halves as compared to p_0 in time interval t_s in linear acoustics without regard for the $2T$ stage. The further decrease in this pressure in times longer than t_s depends on the degree of wave nonlinearity. Here, we speak about a slow decrease in p at $t \gg t_s$ to the values that are lower than half initial pressure p_0. The degree of nonlinearity is characterized by ratio p/B, where $B = 1.8$ Mbar is the bulk modulus of gold. In the linear limit during planar one-dimensional propagation, the pressure in the first characteristic of wave RF$^+$ (iii) remains constant after the twofold decrease from p_0 to $p_0/2$.

When nonlinearity is taken into account, compression wave CW$^+$ (i) is broken after some time to form SW in gold [15]. After wave breaking, rarefaction wave RF$^+$ (iii) gradually “sits down” on the SW front, since the flow behind SW is subsonic. Compression wave CW$^+$ (i) at this stage degenerates into a so-called “triangle” SW. Sound dispersion gradually increases the length of the triangle occupied by wave CW$^+$ (i). The point is that the velocity of sound behind the SW front near SW is higher than at a long distance from the SW front. This is the case, since the pressure near SW in the instantaneous profile is higher. The SW amplitude in gold decreases in time because of sound dispersion and the expansion of the compression layer behind SW.

The emission of a pair of successive waves, i.e., CW$^+$ (i) and RF$^+$ (iii), from hot layer d_T occupied by the entropy mode was described in [27, 58]. A pair of high-pressure wave (i) and low-pressure wave (iii) is clearly visible in x, t diagrams [59, 60]. The x, t show how the spatial separation of waves (i) and (iii), on the one hand, and the near-contact entropy mode “frozen” in the substance, on the other, occurs in time t_s. Fast modes (i) and (iii) go to the volume and the hot layer is retained at CB. Since we are interested in the near-contact phenomena, we do not discus the fate of waves (i) and (iii) and only note that the problem of laser SW and its decay is interesting. There are important problems related to the splitting of SW into elastic and plastic waves (see [60] and Refs. therein).

It is important that, at $d_T < \infty$ during expansion into rarefaction wave (iii), the pressure nonmonotonically decreases to the external pressure, as in the self-similar situation. During expansion into vacuum, the pressure at CB is zero, and a negative-pressure region exists between CB and the head characteristic of the rarefaction wave. In other words, nonmonotonic behavior takes place: a minimum, where pressure is negative, appears instead of a smooth change in pressure from the maximum value to zero. This minimum is caused by the fact that $d_T < \infty$, which means that the initial (after heating) high-pressure profile induced by fast heating is limited in thickness. Therefore, the velocity of expansion into vacuum $u \approx p/Z$ decreases with decreasing pressure p along the profile. Hence, the material particles located closer to CB fly to vacuum faster than the particles that are farther from CB. Thus, the condensed matter is extended and a gradient appears; according to this gradient, the pressure near CB increases when the distance to CB decreases. Since the pressure on CB is zero, the pressure near CB becomes negative [27, 58].

The instantaneous pressure profile (time t) has minimum $|p_{\min}(t)|$, where pressure is negative. The point of the minimum moves into the gold volume in time and $|p_{\min}(t)|$ increases from zero to maximum $|p_{\min}|_{\max}$ [27, 58]. Then, $|p_{\min}(t)|$ does not change in the linear acoustic approximation. In this approximation, we have $|p_{\min}(t)| = p_0/2$. As noted above, p_0 is the maximum pressure in the $p(x, t)$ pressure profile for $\tau_L < t_{\mathrm{eq}} < t \ll t_s$. $|p_{\min}|_{\max}$ is reached in a certain time on acoustic time scale t_s.

This near-contact pressure gradient retards expansion velocity $u_{CB}(t)$. Therefore, the velocity of CB motion toward vacuum $u_{CB}(t)$ decreases in time. The deceleration of CB lasts for a time on the order of t_s until rarefaction wave (iii) of thickness d_T leaves hot layer d_T. If velocity $u_{CB}(t)$ vanishes because of retardation, the continuity of the condensed phase is retained, CB stops, and waves (i) and (iii) continue their motion from CB. This is the end of retardation, when tension stress $|p_{\min}|_{\max}(F_{\mathrm{abs}})$ is lower than the strength of the condensed phase.

$|p_{\min}|_{\max}(F_{\mathrm{abs}})$ increases with absorbed energy F_{abs}. The nucleation of cavitation bubbles begins when stress $|p_{\min}|_{\max}(F_{\mathrm{abs}})$ exceeds the strength of the condensed matter. The corresponding value of F_{abs} is called the ablation, cavitation, or spallation threshold $F_{\mathrm{abs}|\mathrm{abl}}$. The ablation threshold is higher than the melting threshold. Therefore, nucleation occurs in a liquid and cavitation is correspondingly discussed. The frontal ablation and the back spallation in films were compared in [15, 58], and the laser-irradiated film surface is frontal.

Nucleation sharply changes the relation between density and pressure, and a one-phase equation of state changes into a two-phase vapor–liquid equation of state. Moreover, the appearance of spallation pulses moving to the right and left from a nucleation layer is related to nucleation and a sharp decrease in the tensile stress [15, 58]. As a result, the profile of rarefaction wave RF^+ (iii) changes strongly, whereas the profile of compression wave CW^+ (i) preceding this wave remains unchanged. The change in the RF^+ (iii) profile consists in the fact that a low-stress (near-zero-stress) region consisting of condensed fragments and vapor appears instead of the negative pressure well running along a continuous tensioned condensed phase at the velocity of sound. The sharp deceleration of the expansion velocity terminates in this fragmented layer, and the mode that approximately corresponds to the coasting flight of a substance appears.

Our estimates and calculations from [61, 62] demonstrate that the case near the ablation threshold in vacuum is of no interest for the problem of fragmentation into droplets or the droplet condensation of the vapor–liquid or vapor laser ejection of gold into water: nanoparticles are almost absent at $F \approx F_{\mathrm{abs}}$ (this is the threshold for ablation in vacuum) [63, 64]. The problem of the formation of gold nanoparticles in water corresponds to the F_{abs} energies that are significantly higher than the ablation threshold in the case with vacuum. In this situation, the critical temperature is approached, the fragmentation layer is thick, and it includes the mass that is comparable with the layer d_T mass (which follows from the calculations given below). However, at $F \approx F_{\mathrm{abl}}$, the mass of fragments is small as compared to the layer d_T mass. Thus, significant part of the layer d_T mass passes through rarefaction wave RF^+ (iii) and flies under its own inertia in the conditions under study when absorbed energy is significantly higher than ablation threshold in case with vacuum.

Large mass $\sim d_T$ separates from the bulk gold because the temperatures in this mass are high and, hence, the cohesion bonding is weak. Separation is caused by fragmentation. Namely, the mass 5–I accretes (fall down) onto the boundary 5 of atmosphere *4* in Figs. 2 and 3. Accretion occurs in the presence of water, which retards free expansion and, hence, creates atmosphere *4*. Because of water retardation, CB and the atmosphere move more slowly than fragmented substance 5–I. It is important that the velocity of sound in the two-phase region is determined by the vapor pressure and is rather low. Therefore, an effective accretion flux is supersonic. When reaching the atmosphere, the liquid elements of the fragmented substance "does not know" about it.

Note that the nucleation (ablation) threshold increases slightly in the presence of water, which is associated with the increase in the pressure at the contact ($p_{CB} \approx 3$–7 GPa (Eqs. (6), (11)) instead of zero in the case of vacuum). The acoustic impedance of water is low as compared to that of gold; therefore, the change in the ablation threshold is small.

4. EQUATIONS OF ONE-DIMENSIONAL TWO-TEMPERATURE HYDRODYNAMICS

We consider the action of an ultrashort laser pulse on a flat metallic surface submerged in a transparent liquid. Light passes through the liquid and is absorbed in the skin layer of the metal. No optical breakdown takes place, since the radiation intensities are moderate and the pulse durations are short ($\tau_L = 0.1$–1 ps). The absorbed energies are $F_{\mathrm{abs}} = 400$–1000 mJ/cm^2. For definiteness, we analyze the gold–water pair. The thermomechanical ablation threshold during an analogous action on gold in a gas or vacuum is approximately $F_{\mathrm{abs|abl|vac}} = 100$ mJ/cm^2 [15, 27, 52].

To analyze the situation qualitatively described in the previous sections, we now use one-dimensional two-temperature (2*T*) hydrodynamic code 2*T*HD recorded for the Lagrangian coordinate. The corresponding set of equations has the form

$$\rho(x_0,t)\frac{\partial x(x_0,t)}{\partial x_0} = \rho_0, \tag{13}$$

$$\rho_0\frac{\partial u}{\partial t} = -\frac{\partial P(x_0,t)}{\partial x_0}, \tag{14}$$

$$\frac{\partial x(x_0,t)}{\partial t} = u(x_0,t), \tag{15}$$

$$\rho_0\frac{\partial (E_e/\rho)}{\partial t} = -\frac{\partial q}{\partial x_0} - \dot{E}_{ei} + \frac{\rho_0}{\rho}Q - P_e\frac{\partial u}{\partial x_0}, \tag{16}$$

$$\dot{E}_{ei} = \frac{\rho_0}{\rho}\alpha(T_e - T_i), \quad q = -\frac{\rho\kappa\partial T_e}{\rho_0\,\partial x_0}, \tag{17}$$

$$\rho_0\frac{(\partial E_i/\rho)}{\partial t} = \dot{E}_{ei} - P_i\frac{\partial u}{\partial x_0}, \tag{18}$$

$$Q = \frac{F_{\mathrm{abs}}}{\sqrt{\pi}\tau_L\delta}\exp\left(-\frac{t^2}{\tau_L^2}\right)\exp\left(-\frac{x}{\delta}\right)\theta(x). \tag{19}$$

Here, Eq. (13) describes the law of conservation of mass and the trajectory $x(x_0, t)$ of a material particle with Lagrangian coordinate x_0; $x(x_0, t = -\infty) = x_0$ and ρ_0 is the initial density. Equation (14) represents the law of conservation of momentum, where $u(x_0, t)$ is the Lagrangian particle velocity. Equation (15) is the kinematic condition. The law of conservation of energy is written separately for the electron and ion subsystems. The energy balance in the electron subsystem is described by Eq. (16) (see [9]). The power of the energy exchange between the electron and ion subsystems per unit volume and the electron heat flow are given by Eqs. (17). The energy balance in the ion subsystem is described by Eq. (18). The heating power per unit volume due to the absorption of laser pulse radiation is given by Eq. (19), where δ is the skin layer thickness and τ_L is the laser pulse duration. Formula (19) with function $\theta(x) = 1$ at $x > 0$ and $\theta(x) = 0$ at $x < 0$ is valid for ultrashort moderate-intensity pulses, when the displacement of CB during the pulse duration may be neglected. At the initial time, CB is at point $x = 0$. An absorbing substance is located to the right, at $x > 0$.

The solution of the set of equations is known to need the data that describe the thermodynamics of the system (equation of state), electronic thermal conductivity κ, and the electron–ion energy exchange (knowledge of coefficient α) through, from 2*T* to 1*T* states. We use modern data for the calculations given below. The thermodynamics that describes both 2*T* and 1*T* states is based on the rough representation of the free energy of gold as a sum of the free energies of the ion and electron subsystems [65–67]. Here, the ionic part is taken from the wide-range equation of state [46–48]. In the 2*T*HD calculations, water is described using approximation (12). In the 2*T*HD code, the thermal conductivity of water is neglected. An effective interatomic potential, in which water molecules are represented as points, was developed for a molecular dynamics (MD) simulation. In MD, the thermal conductivity of water is low but finite and is related to the vibrational motion of molecules.

The high thermal conductivity of gold plays an important role, which is especially important at the 2*T* stage. This thermal conductivity in the 2*T*HD calculations was taken according to the models in [18, 19, 68–70]. Coefficient α, which characterizes the rate of electron–ion exchange, is also an important parameter [18, 69–71]. In the calculations given below, we use the approximation

$$\begin{aligned}\alpha(\tau, T_e)[\mathrm{W\,K^{-1}\,m^{-1}}] &= (\rho/\rho_0)^{5/3}\\ &\times\left(0.2 + \frac{4.3}{K_\alpha}\frac{T_{\mathrm{eV}}^{3.6}}{1 + T_{\mathrm{eV}}^{3.5} + 0.9T_{\mathrm{eV}}^{4.1}}\right)10^{17}.\end{aligned} \tag{20}$$

Here, electron temperature T_{eV} is given in electron volts, and parameter K_α determines quantity (20) at high T_e temperatures.

At low T_e, approximation (20) begins with an experimental value of 0.2×10^{17} W K^{-1} m^{-3} [3]. The authors of [71] considered the variation of parameter K_α in Eq. (20) in the range from 1 to 6. The values of K_α about 1 correspond to an $\alpha(\rho_0, T_e)$ relation close to that given in [72]. At $K_\alpha \approx 1$, function (20) increases by an order of magnitude with temperature T_e. At $K_\alpha \approx 4$–6, the increase in $\alpha(\rho_0, T_e)$ with T_e above 10 kK is much weaker (by a factor of 1.5–3) as compared to α at room temperature. Ng [73] thinks that his experimental data count in favor of a small increase in parameter α with temperature T_e. At $K_\alpha \approx 1$, the electron–ion relaxation in gold is faster than that at $K_\alpha \approx$ 4–6. Below, we will consider the version at $K_\alpha = 1.15$.

5. RESULTS OF ONE-DIMENSIONAL CALCULATION AT $F_{\mathrm{abs}} = 400$ mJ/cm^2

5.1. Early Stage, 2T Relaxation

The two-temperature (2*T*) relaxation, which proceeds in the first several picoseconds after a subpicosecond action on gold, is identical to that in the case of vacuum. Figure 10 shows how the electron ($T_e(x, t)$) and ion ($T_i(x, t)$) temperatures move toward each other. They move toward each other simultaneously with heat propagation to the gold target volume. At a time of about 10 ps, the melting zone motion is still supersonic: in the time interval 2–15 ps, the melting zone (*m*) travels from $x \approx 60$ nm to $x \approx 160$ nm (cf. Figs. 10 and 11). At a time of 15 ps, the head characteristic of the rarefaction wave is at a distance of 60 nm

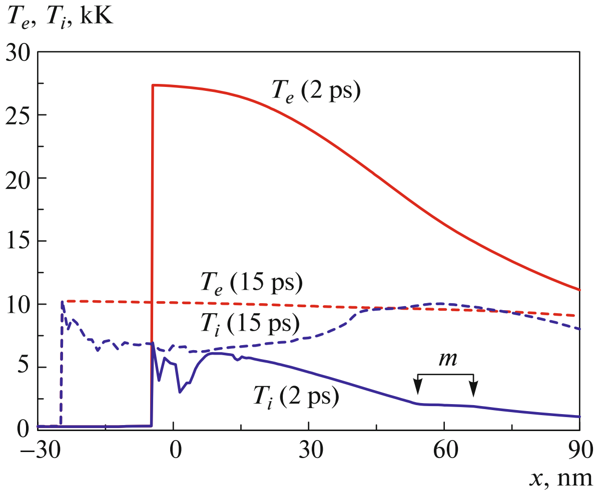

Fig. 10. (Color online) Electron–ion relaxation kinetics. Early stage of expansion of gold heated by a laser pulse. Here and in the next figure, the absorbed energy is F_{abs} = 400 mJ/cm^2 and the duration is τ_L = 0.1 ps. The time is measured from the maximum of the pulse intensity in the form of a Gaussian function in time (Eq. (19)). Bracket m indicates the position of the melting zone at a time of 2 ps.

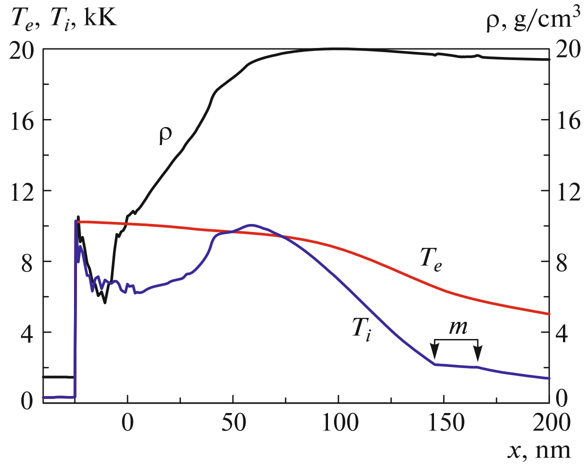

Fig. 11. (Color online) Profiles of the electron (T_e) and ion (T_i) temperatures in an almost one-temperature (1/T) stage, t = 15 ps. Nevertheless, the difference between the local temperatures is noticeable (see text).

from the initial position of CB. At the 2T stage, the velocity of sound increases slightly as compared to 3 km/s because of the additional electron-pressure-induced elasticity. The melting zone (zone m) in Figs. 10 and 11 consists of a mixture of solid and liquid phases. The melting patterns in hydrodynamics and molecular dynamics were compared in [74] (also see [60]). These patters were shown to agree with each other in integral parameters (temperature profile, fraction of liquid phase). Below, we present the results of MD simulation of gold ablation into water Note that meting at the early stage occurs under compression wave pressure. Therefore, the melting zone temperature is higher than the temperature of the triple point [60].

The temperature in Figs. 10 and 11 and the density in Fig. 11 undergo a sharp drop at the CB between gold and water. As noted above, we neglect the low thermal conductivity of water in the 2THD calculation. The thermal conductivity of water at the thermal quasi-vibrations of molecules is automatically taken into account in the MD code.

The large difference between T_e and T_i (several tens of kilokelvins) at the first picoseconds (Fig. 10, profiles for 2 ps) levels off by 5–10 ps. By that time, the heat energy transferred to ions is several times higher than the heat energy retained in electrons. Nevertheless, the difference between local temperatures T_e and T_i remains noticeable even at 15–20 ps (see Fig. 11). In the rarefaction wave region (to the left of the maximum density in Fig. 11), this difference is related to very strong hydrodynamic expansion of the gold flow to a high-amplitude rarefaction wave. In this wave, the density drops to the values that are close to the critical density of gold (5.3 g/cm^3; see caption to Fig. 4). Tension causes the consumption of internal energy for expansion. The influence of the expansion flux on the temperature difference can be spoken about at the stage $t < t_s \approx 50$ ps. At the stage $t > t_s$, the rarefaction wave gradually leaves heating layer d_T. Temperatures T_e and T_i are low outside this layer.

Apart from the rarefaction wave zone, the difference between temperatures T_e and T_i in Fig. 11 is noticeable in the melting region, which is related to the energy consumed for melting.

5.2. Formation of Atmosphere Because of Water Drag and the Accretion-Induced Increase in the Atmosphere Mass and Momentum

Figures 12–14 illustrate the essence of the dynamic picture of gold expansion. The play of acoustic waves and CB deceleration are visible in these figures. As in the case of expansion into vacuum, a rarefaction wave and a compression wave are present (see Section 3). These waves are separated by the head characteristic of the rarefaction wave, which is at the high pressure maximum (another maximum of p exists at the SW front). The instantaneous position of the pressure maximum approximately coincides with the low maximum of density (compression in density is low). The maximum of density is slightly to the right of the maximum of p because of a decrease in the temperature into the gold volume.

The deceleration of CB also takes place during expansion into vacuum. Therefore, according to the principle of inert mass–gravitational mass equivalence, there exists an effective gravitational field, the free fall vector of which is directed from a high-density

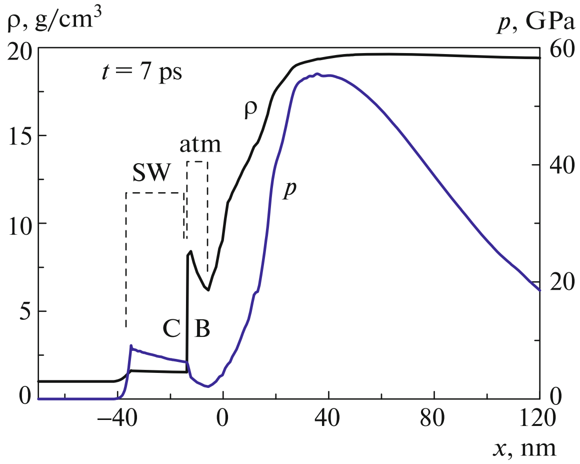

Fig. 12. (Color online) Profiles of density and the total pressure, which enters into Eq. (14). SW in water, shock-compressed water layer, water–gold contact (CB), and atmosphere (atm) of gold heaped on stopping water are shown. Numeral *4* in Fig. 2 corresponds to the atmosphere. The rarefaction wave is to the left of the maximum pressure, and the compression wave is to the right.

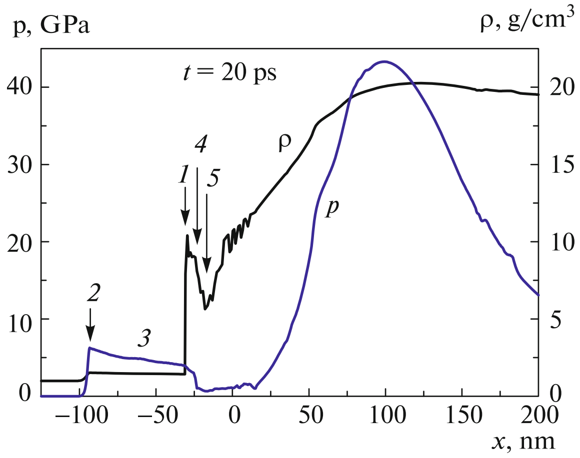

Fig. 13. (Color online) The same structure as in Fig. 12 at a time $t = 20$ ps. The structure components are designated by the numerals explained in Fig. 2. The decrease in the density and the pressure between atmosphere boundaries *1* and *5* is caused by effective gravitation g (see Fig. 3). The density oscillations inside the rarefaction wave correspond to the initial stage of nucleation.

medium to a low-density one. This means the presence of Rayleigh–Taylor instability (RTI) of CB [39, 41, 42, 50, 51].

If a medium is solid, its strength hinders the development of RTI (see Appendix A). If a medium is liquid, the length of the modes that can grow in a relatively short deceleration time (shorter or comparable with t_s) λ_{RT} is estimated to be small as compared to heating layer thickness d_T, $\lambda_{RT} \ll d_T$. This estimate does not take into account surface tension σ and kinematic viscosity ν. When σ and ν are taken into account, minimum scale $\lambda_{\rm stab}$ that is comparable with thickness d_T under our femtosecond-pulse conditions appears. Thus, RTI may be neglected during expansion into vacuum (see Appendix A). Indeed, on the one hand, we have $\lambda_{RT} \ll d_T$; on the other, $\lambda_{RT} > \lambda_{\rm stab} \sim d_T$.

In the case of vacuum, deceleration $g(t)$ is operative until a spallation plate is separated. For the expansion of gold into water, the deceleration stage is longer; it is not bounded by time interval $t_{\rm nucl}$; we have $t_{\rm nucl} \sim t_s$ near nucleation threshold $F_{\rm abs}|_{\rm nucl}$; and $t_{\rm nucl}$ vanishes if absorbed energy $F_{\rm abs}$ exceeds the nucleation threshold by several times. The strength of gold is low under strong heating. Heating is strong if energy $F_{\rm abs}$ is higher than threshold $F_{\rm abs}|_{\rm nucl}$ by several times, and this is not the case in the formulation of the problem under study. Correspondingly, surface tension σ becomes very low or zero, since we approach or even exceed the temperature of the critical point at high $F_{\rm abs}$ energies. The noticeable retardation of RTI is related to viscosity ν (see Appendix B for viscosity under our conditions). Below, we will study this problem. Now, we return to an analysis of the one-dimensional dynamics.

The expansion of rapidly heated gold creates SW in water (Figs. 13, 14; point *2*). SW runs into water and a rarefaction wave runs into gold because of the decay of the gold–water discontinuity with a high pressure in gold (initial pressure in water is neglected). A shock-compressed water layer is located between SW and CB (Fig. 12, SW). The deceleration of CB becomes noticeable as the thickness of the gold layer covered by the rarefaction wave increases with respect to thickness d_T. The following pressure gradient appears because of the deceleration of CB: the pressure first decreases from the value at the SW front to p_{CB} at CB. The decelerating CB generates a decaying SW. The pressure on SW, the compression in SW, and the SW and water velocities behind SW decrease monotonically in time.

The pressure at the contact (p_{CB}) is positive and decreases gradually in time. The instantaneous coordinate dependence of the pressure is continuous at CB. CB deceleration g is the same in the vicinity of CB for water and gold, since water is in close contact with gold at CB. Therefore, a pressure gradient jump takes place at CB because of a sharp density jump at CB (see Figs. 12, 13). The ratio of the gradients $dp/dx = -\rho|g|$ is equal to the ratio of the densities at CB. Thus, the pressure in the atmosphere–shell (Figs. 12–14, *1*–*4*–*5*) drops sharply. At upper atmosphere boundary *5*, pressure is maintained due to pressure in the rarefaction wave tail and to the momentum that moves from the wave to the atmosphere.

The substance in the rarefaction wave tail moves faster than CB and the atmosphere because of the

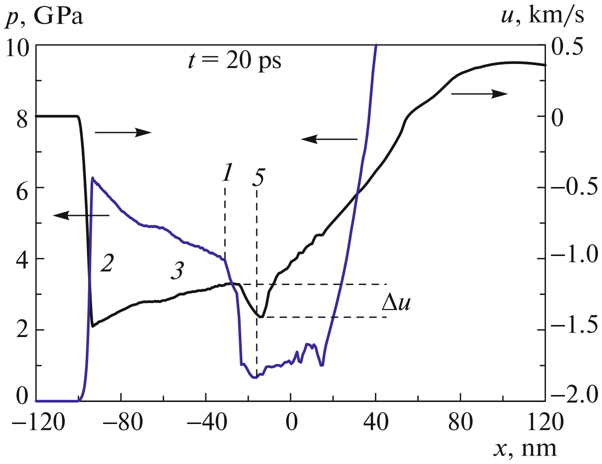

Fig. 14. (Color online) Jumplike drop Δu in the expansion velocity at "upper" (with respect to free fall acceleration vector g in Fig. 3) boundary *5* of atmosphere *4* (numerals are explained in Fig. 2). The deceleration of high-density gold atmosphere *1–4–5* is provided by the sharp pressure drop in the atmosphere layer (see Figs. 12, 13).

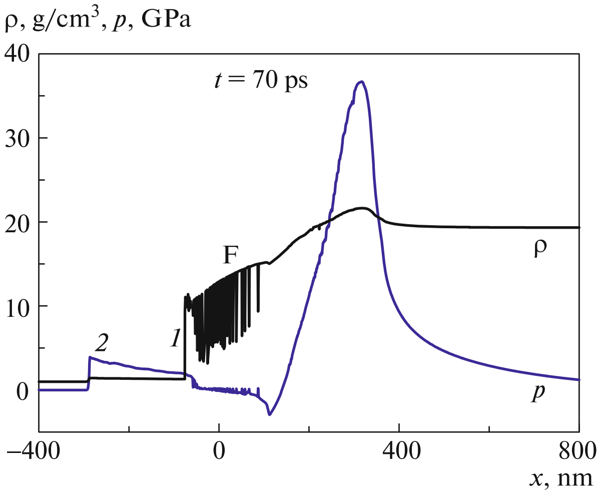

Fig. 15. (Color online) Formation of extended nucleation zone F (serrated segment of profile ρ) when nucleation threshold F_{abs} is exceeded by several (approximately four) times. Two-phase mixture segment F transforms gradually into gold foam. The volume fraction of the liquid phase in foam is low. The calculation at τ_L = 100 fs and F_{abs} = 400 mJ/cm^2 (see Section 5).

deceleration of CB. The appearance of velocity jump Δu at upper boundary *5* of atmosphere *4* is related to this factor and the supersonic motion of the substance in the rarefaction wave tail (see Fig. 14).

The pressure in water is well below the pressure in the compression wave running to the right, into the gold volume in Figs. 12–14, which is caused by the large difference between the acoustic impedances of water and gold (Z_{Au}); we have $Z_{\text{Au}}/Z_{\text{wt}} = 40$ under normal conditions. The pressure in water was estimated in Section 2 (see Eqs. (6), (11)), and these estimates agree with the values presented in Figs. 12–14. The influence of water on the rarefaction wave in gold is restricted by the atmosphere. Behind atmosphere boundary *5*, gold does not know about water. Since the impedance of water is low, the atmosphere is thin: its thickness is much smaller than heating layer thickness d_T at the early and medium stages of expansion.

Part on the order of unity of the fragmented heating layer accumulates gradually in the atmosphere, and the atmosphere thickness becomes comparable with d_T. This situation occurs at the late stages of deceleration. Here, the atmosphere thickness is substantially smaller than the path traveled by the atmosphere during deceleration.

5.3. Nucleation and Medium Stage of Contact Deceleration

The beginning of nucleation is visible in Fig. 13: the serrated segment at the end of the rarefaction wave in the density profile. Nucleation begins in the rarefaction wave tail at a certain distance from the thin atmosphere. As the rarefaction wave moves, the nucleation layer grows (see the density profiles in Figs. 13 and 15). The nucleation layer thickness is 150 nm at a time of 70 ps (see Fig. 16). Then, the two-phase liquid–vapor layer undergoes substantial expansion in time, which is related to the coasting flight of the substance of the two-phase layer and to velocity gradient du/dx in this layer. Below, we will compare the results of the 2*T*HD and MD calculations and make conclusions regarding the three-dimensional structure of the liquid–vapor region.

Gold in the nucleation layer is strongly heated (see Fig. 16), and the temperature in this layer increases from 3 to 7 kK. At such temperatures, the strength decreases to low values. Therefore, no substantial negative pressures appear in the melt before nucleation. Negative pressures appear when the local temperature decreases because of the gradual motion of the rarefaction wave from the heating layer of thickness d_T. The minimum in Fig. 16 ($p < 0$) is located at a depth of 112 nm, where the temperature decreases to 3 kK.

A two-phase vapor–liquid mixture forms as a result of nucleation. The pressure in the mixture is low if it is compared with the pressure in the compression wave in gold (see Figs. 15, 16). The two-phase pressure is determined by the saturated-vapor pressure in the hot part of the mixture that is adjacent to the atmosphere. As follows from Fig. 4, the gold vapor pressure is about 0.1 GPa at T = 6 kK. Small negative values of p are retained in the cold part of the two-phase layer because of the weak tension resistance of foam due to surface tension (see Fig. 16) [22, 25]. The vapor–liquid layer expands in the mode that is close to dust expansion: the pressure, the pressure gradient, and the velocity of sound gradient in this layer are low. Corre-

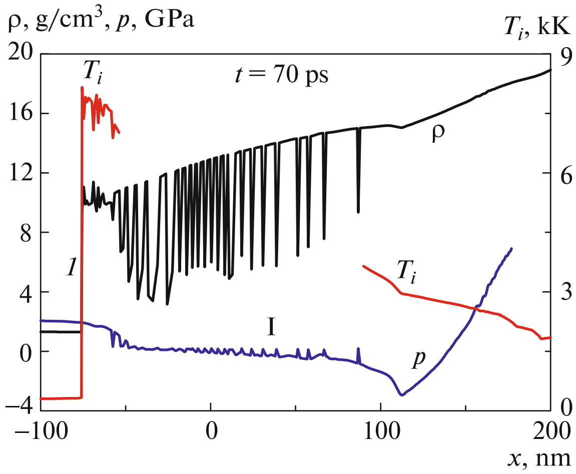

Fig. 16. (Color online) Atmosphere and nucleation zone taken from Fig. 15 are to the right of contact *1*. The atmosphere is heated to the near-critical temperature (see Fig. 4).

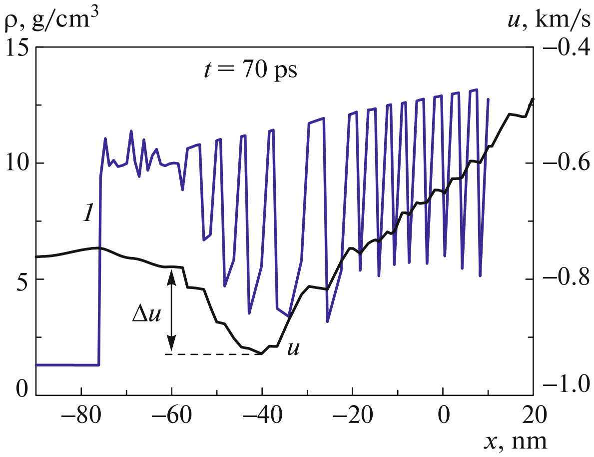

Fig. 17. (Color online) Sharp decrease in the expansion velocity during the collision of the vapor–melt mixture substance with the upper atmosphere boundary. Δu = 150 m/s (cf. with Fig. 14, where this velocity decrement is 240 m/s).

spondingly the velocity distribution over the Lagrangian coordinate is retained during expansion: the velocity is "frozen" in the Lagrangian coordinate.

As noted above, the atmosphere moves more slowly than the two-phase substance near the atmosphere because of water deceleration. The velocity of sound in the mixture is low; therefore, the mixture flux onto the atmosphere is supersonic; that is, the velocity of sound in the mixture is smaller than velocity difference Δu in Fig. 17. Hence, the two-phase substance does not know about the atmosphere. Thus, upper atmosphere boundary *5* is represented by SW, which separates the atmosphere from the accretion flux to it (see Figs. 2, 3, 12–14). Figures 17 and 18 show the pressure and velocity profiles inside this SW. The atmosphere thickness is 15–20 nm at a time t = 70 ps, and the SW width is approximately the same.

The difference between the pressure at contact *1* in Fig. 18 and the pressure in the inflowing mixture is approximately 1.8 GPa. Using the CB trajectory, we determine the CB velocity and deceleration $g(t)$. We have $g \approx 4.3 \times 10^{14}$ cm/s² at t = 70 ps. The atmosphere weight gives the pressure difference

$$\Delta p_{\rm atm} = \rho g h$$

between the boundaries *1* and *5* of atmosphere *4* (see Figs. 2, 13). Substituting atmosphere density $\rho \approx$ 10 g/cm³ and thickness h = 15–20 nm, we find $\Delta p \approx$ 1 GPa.

We now estimate the pressure increment in SW forming boundary *5* of atmosphere *4*. To this end, we write the law of conservation of mass

$$\Delta u + D = CD,$$

where Δu is the inflowing mixture velocity in the coordinate system related to the atmosphere; D is the SW velocity in this coordinate system; $C = \rho_2/\rho_1$ is the degree of compression in SW; and ρ_2 and ρ_1 are the substance densities at upper boundary *5* of the atomic transition and in the mixture in front of SW, respectively. The law of conservation of momentum gives

$$\Delta p_{SW} = \rho_1 \Delta u(\Delta u + D),$$

where Δp_{SW} is the change in the pressure in SW. Substituting Δu = 150 m/s (see Fig. 17) and $C \approx 2$, we find $\Delta p_{SW} \approx 0.2$ GPa. However, the sum $\Delta p_{\rm atm} + \Delta p_{SW} \approx$ 1.2 GPa is smaller than 1.8 GPa, which is associated with the estimation error. The pressure difference in front of and under the atmosphere is seen to be mainly related to the atmosphere weight.

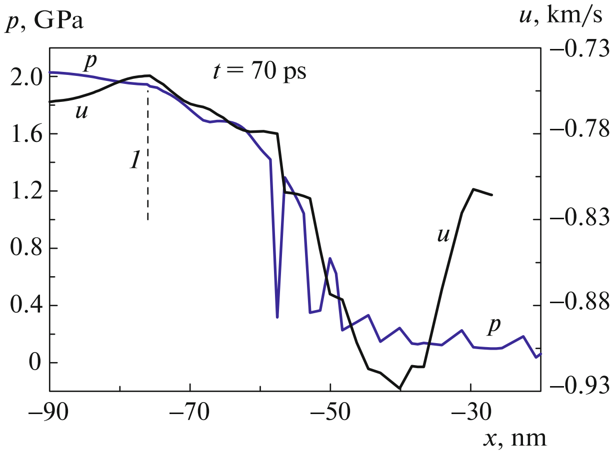

Fig. 18. (Color online) Structure of atmosphere and SW, which forms the upper atmosphere boundary. Vertical mark *1* indicates instantaneous position of CB.

Cavities are closed in the SW, and the two-phase vapor–melt mixture passes to the atmosphere and returns to a single-phase liquid state. In Fig. 18, the pressure in this state is higher than the critical pressure of gold.

The volume fraction of the liquid phase in the mixture decreases gradually due to expansion. The state of liquid with bubbles transforms into the state of foam, and a mixture of droplets in vapor then forms after breaking membranes and filaments in the foam [22, 29]. Surface II in Fig. 2 separates foam region 5–II from the droplet mixture region I–II. As noted above, the two-phase mixture region can be approximately described as the region in the coasting flight. However, the velocities of Lagrangian particles in the mixture change slowly because of the weak interaction caused by the surface tension of membranes and filaments [22, 29]. Through this interaction, part of the foam is mechanically related to the atmosphere and the other part, to the bottom of the forming crater. As a result, the zero of the velocity oriented along the main motion (along x) turns out to be inside the mixture.

The atmosphere is gradually decelerated and stops eventually. The foam in region 5–II and droplet substance II–I join the atmosphere layer at these times. The foam of the layer from boundary I to the crater bottom are retained on the target. Point I inside the foamed layer is shown in Fig. 16. The zero of the foam velocity is associated with boundary I in Fig. 2.

At longer times, SW is damped in water and its velocity decreases to the velocity of sound in water (1.5 km/s). Note that the average SW velocity in the time interval $0 < t < 70$ ps in water is 4 km/s and the average Mach number is 2.7. The CB velocity decreases to 1–10 m/s at times of several fractions of a microsecond. The calculation described in this section for $F_{\text{abs}} = 400$ mJ/cm^2 was performed to a time of 200 ns. At $t = 200$ ns, CB travels 2.8 μm and SW in water travels 340 μm.

To decrease the amount of calculations at such large scales and times, we reject the part of gold belonging to the substitution to the right of boundary I in Figs. 15 and 16 beginning from time $t = 70$ ps. An impermeable fixed wall, which confines vapor inside the space between the atmosphere and the crater bottom, is placed at the cut of the calculation. The rejection of the substance on the right of wall I in Figs. 15 and 16 weakly affects the motion dynamics of the atmosphere and the adjacent two-phase mixture. We made the same manipulations for the MD simulation presented below.

Owing to cutting a chain of Lagrangian cells at point I, we will not trace the compression wave that moves deep into the gold volume (see Fig. 15). The compression wave is broken soon after the time shown in Fig. 15. A triangular SW forms in gold in a short time and a rarefaction wave sits down on its front. Thus, the pair of waves consisting of a rarefaction wave and a compression wave in Figs. 12–15 degenerates into a pair consisting of a rarefaction wave and SW [15, 60]. Sound dispersion extends the fan of characteristics of the rarefaction wave, which covers the shock-compressed gold layer, and this wave smoothly decreases the SW amplitude.

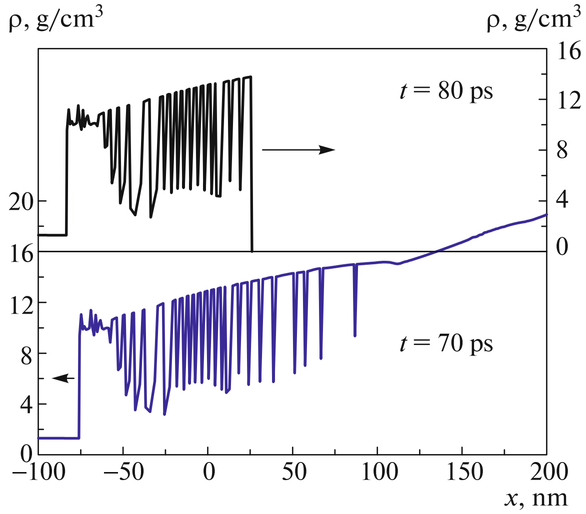

Fig. 19. (Color online) Exclusion of the passive part of foam and the gold volume to save computational resources. (bottom) Density profile before exclusion and (top) profile after exclusion. The decrease in the calculation segment weakly affects the atmosphere and SW motion in water.

Figure 19 shows the density profiles before cutting the right part of the calculation segment, at a time of 70 ps, and after cutting, at 80 ps. Our tests demonstrate that the presence or absence of the right part only weakly affect the dynamics of the left part, i.e., the SW dynamics in water and the dynamics of CB, atmosphere, and foam adjacent to atmosphere.

5.4. Late Stages of Contact Deceleration

Figure 20 illustrates how SW decays in water at the beginning of the subnanosecond time interval. The atmosphere expands due to, first, a decrease in the rate of deceleration g of CB and, second, mass accumulation from the two-phase mixture. In the time interval 70–250 ps (see Fig. 20), SW (mark *2*) decreases its velocity from 3.55 to 3.0 km/s, the deceleration of CB decreases from 43×10^{13} to 8.8×10^{13} cm/s^2, the CB velocity decreases from 750 to 410 m/s, and the average gold density in the atmosphere increases from 10.2 to 11.7 g/cm^3. The increase in the atmosphere density is caused by a decrease in the pressure on CB and a decrease in the atmosphere temperature from 7.60 to 6.44 kK. The cooling of the atmosphere in the 2*T*HD calculation is associated with the attachment of cold foam to the atmosphere due to the atmosphere accretion of foam (recall that the thermal conductivity of water in the 2*T*HD calcu-

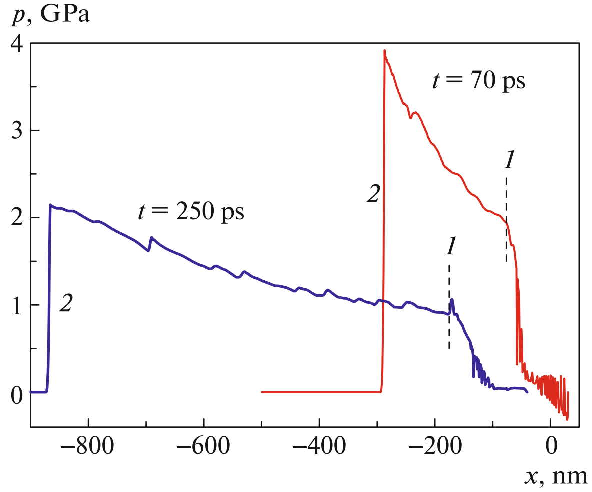

Fig. 20. (Color online) Middle stage of SW propagation and decay (mark *2*) in water. Decay is caused by gradual deceleration of the "piston" pushing SW. The piston is gold–water CB (mark *1*).

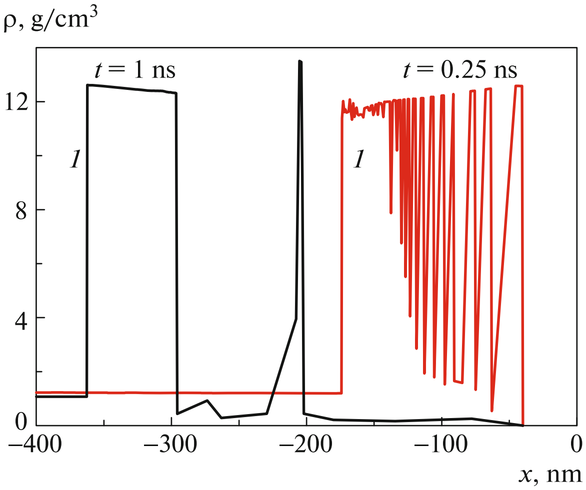

Fig. 21. (Color online) Density profile evolution from the state of atmosphere plus foamed mixture to the state with exhausted reserve.

lation was neglected). In the MD calculations, we take into account both the thermal conductivity of foam (heat removal through membranes and filaments) and the vibrational thermal conduction through water molecules.

The change in the density distribution in the time interval 0.25 ns < t < 1 ns is illustrated in Fig. 21. The SW coordinate in water increases from 870 to 2850 nm in this interval. The SW velocity decreases to 2.5 km/s and the compression of water in SW is 20% at t = 1 ns. SW is far to the left of the density profile in Fig. 21 and the atmosphere thickness is $h(t = 1 \text{ ns}) = 65$ nm. Therefore, SW is not shown here. Note that the atmosphere thickness increased by a factor of 2–3 in the time interval from 70 ps to 1 ns (cf. Figs. 21 and 17–19). In the time interval 0.25 ns < t < 1 ns, the atmosphere accretion of the two-phase mixture ceases gradually, since the major part of the mixture has precipitated in the atmosphere.

The pressures at SW and CB are $p_{SW}(t = 1 \text{ ns}) = 1.1$ GPa and $p_{CB}(t = 1 \text{ ns}) = 0.22$ GPa = 2200 bar, respectively; that is, the pressure at a far SW is much higher than the pressure at the contact. Temperature $T(t = 1 \text{ ns}) = 5.93$ kK is leveled through the atmosphere thickness. The saturated gold vapor pressure at this temperature is approximately 750 bar (see Fig. 4).

Figures 22 and 23 show the pressure profiles in water at the late stage of CB expansion. Since SW is far, the region with gold on this scale is seen as a weak burst to the left of zero. This burst moves slowly (as compared to the SW velocity) to the left. The flow profiles shown in Fig. 23 are not self-similar. In the relative coordinates, the layer of a sharp decrease in the pressure behind SW becomes thinner as compared to the distance traveled by SW. As is seen from Figs. 23 and 24, the pressure at CB decreases in time faster than the pressure at SW.

In Fig. 24, we compare the time evolution of the pressures at SW and CB. After $t \approx 100$ ps, SW in water decays approximately as $p_{SW} \propto t^{-1/2}$ [75, §102], which is related to sound dispersion (it extends the rarefaction wave located on SW in water). Here, we speak about the approximately triangular part of the pressure and velocity drop behind SW (see Figs. 22 and 23). The water pressure and velocity behind SW are approximately proportional to each other in weakly linear SW. Therefore, the velocity behind the SW front also decays as $t^{-1/2}$. The law $t^{-1/2}$ means that the pushing of SW by a piston (i.e., CB) ceases to play a significant role.

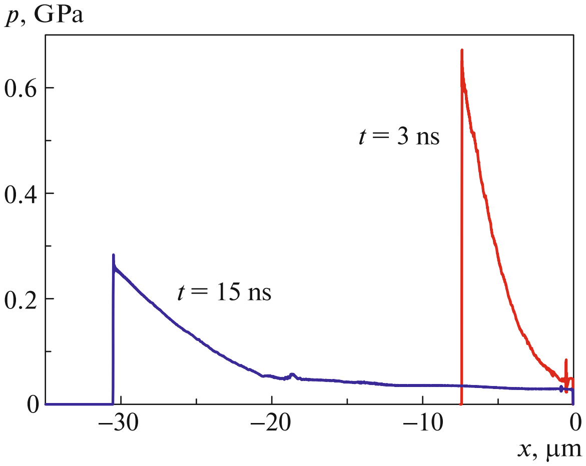

Fig. 22. (Color online) Decrease in the pressure of SW during its 1D propagation. The heating spot diameter is usually several hundred microns; therefore, the 1D approximation is still applicable.

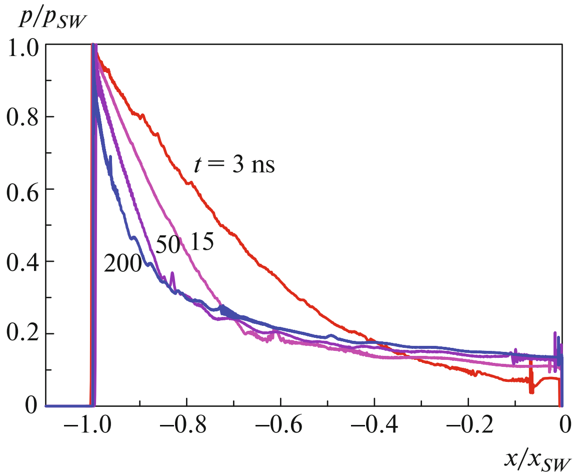

Fig. 23. (Color online) Time evolution of the pressure profile in the coordinates normalized by the current position and the amplitude of SW.

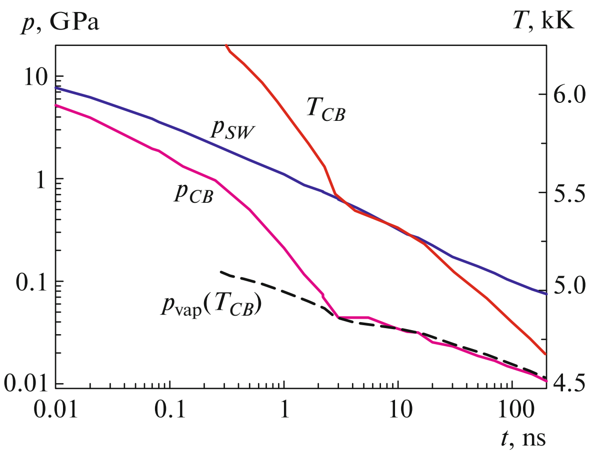

Fig. 24. (Color online) Time dependences of the pressure at SW in water (p_{SW}), the CB pressure (p_{CB}) and temperature (T_{CB}), and the saturated gold vapor pressure at CB at a given temperature ($p_{\text{vap}}(T_{CB})$).

Pressures p_{SW} and p_{CB} are comparable in the subnanosecond time interval, and the pressure at CB then begins to drop, which is related to CB deceleration (see Section 5.5). The situation changes when the decreasing external pressure (water pressure) at CB lowers to the saturated gold vapor pressure at the gold layer temperature: see the motion of the p_{CB} and p_{vap} curves toward each other in Fig. 24. The latter curve was calculated at temperature T_{CB} using the approximation described in the caption to Fig. 4. Then (after reaching p_{vap}), evaporation (if water bounds the gold vapor volume) maintains the pressure at CB at the level of the saturated vapor pressure. As a result, the rate of decrease of the pressure at CB decreases (see Fig. 24).

5.5. Contact Instability

Figures 25 and 26 show the time dependences of the coordinate and the velocity behind SW and CB, respectively. The SW velocity decreases to the velocity of sound in water (1.5 km/s) when the SW pressure decreases well below the bulk modulus of water (2.3 GPa; see Fig. 24). The expansion of SW is traced in Fig. 25 to approximately 400 μm. Then, in experiments with spot diameter $2R_L$ of several hundred microns, SW transforms from a one-dimensional plane wave (dependence of parameters on x) into spherical SW, were parameters depend on radius r measured from the center of the laser heating spot. At $t = 200$ ns, the ratio of the masses of water behind SW and the spalled gold layer is very high, $x_{SW}/h \approx 350 \times 10^3/50 = 7000$.

The displacement of CB is $L = 3$ μm at a time of 200 ns in Fig. 25. By this time, the CB velocity decreases to several m/s; that is, the layer is going to stop (see Fig. 24). In the one-dimensional formulation of the problem, the gold layer (atmosphere) of thickness $h = 50–100$ nm travels a path $L = 60–30$ layer thicknesses before stop. Since CB rapidly picks up speed and then decelerates for a long time, we have

$$L = \int dt \int dt\, g(t) \sim \bar{g}t^2/2,$$

where $\bar{g}$ is the average deceleration and the integrals are taken backward, from stop.

The Rayleigh–Taylor mixing at the boundary of two media having strongly different densities (gold–water) obeys the law $h_+ = \alpha_+ g t^2$ (see Appendix A).

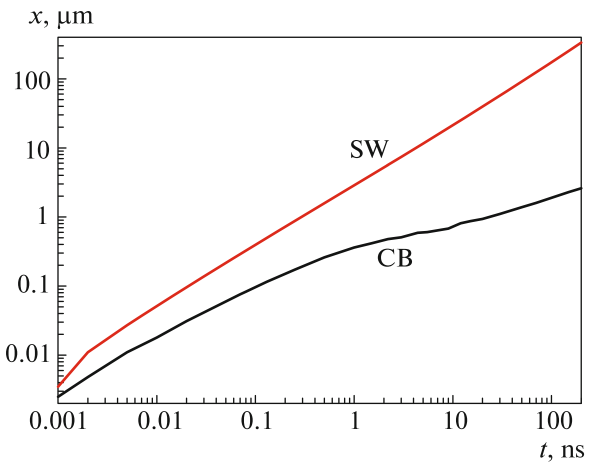

Fig. 25. (Color online) CB or SW displacement vs. time. The CB velocity is high and the CB and SW displacements are comparable in the first several tens of picoseconds. Then, CB is far behind, since the CB velocity decreases rapidly while the SW velocity cannot be lower than the velocity of sound. At 200 ns, these displacements differ by two orders of magnitude. The decrease of the rate of deceleration becomes slightly lower because of a change in the law of decreasing pressure when the saturated vapor pressure is reached (cf. with Fig. 24).

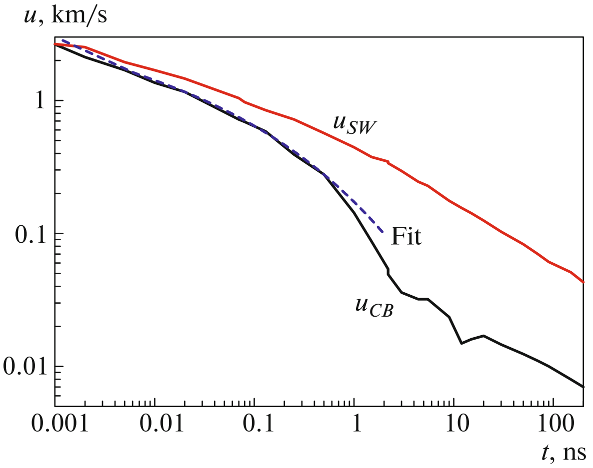

Fig. 26. (Color online) Current water velocity u_{SW} behind the SW front. As SW is damped, this velocity decreases approximately in proportion to the pressure at the SW front (see Fig. 24): $u_{SW} \approx p_{SW}/Z_{\mathrm{wt}}$, where Z_{wt} is the acoustic impedance of water. Curve u_{CB} is the 2*T*HD calculation at $F_{\mathrm{abs}} = 400$ mJ/cm^2. Curve Fit is an analytical approximation (see text).

Here, h_+ is the path traveled by water bubbles into the gold atmosphere from the initial position of the CB surface. The gold layer of thickness h_+ is fragmented into jets and droplets. At time t, the remaining atmosphere $h - h_+$ still retains its continuity and withstands the pressure drop between its inner boundary and the current boundary of bubble penetration h_+. The inner boundary separates the atmosphere and the two-phase mixture (see Fig. 3).

The atmosphere is fully mixed with water when h_+ is comparable with the atmosphere thickness, $h_+ \approx h$. From whence, we can estimate the path $L_{\max}$ traveled by the atmosphere to full mixing, $2\alpha_+ L_{\max} \approx h$, or $L_{\max} \approx h/2\alpha_+$. Since $\alpha_+ = 0.03$–0.05 (see Appendix A), we have $L_{\max} \approx (10\text{–}15)h$; that is, the atmosphere can travel 10–15 thicknesses before its decomposition. Since the one-dimensional calculation indicates the deceleration of the atmosphere after 30–60 thicknesses, the problem of RTI is challenging. The layer can be completely mixed out *before* it stops according to the one-dimensional 2*T*HD code simulation. We first perform a semianalytical analysis of the linear development of RTI against the background of the flow presented in Figs. 25–27. We then perform a complete analysis (without linear approximation) using an MD simulation.

Figure 26 depicts an analytical approximation of the CB velocity (curve Fit). This approximation has the compact form

$$u_{CB} = 4.0554\exp[-0.631255(t_{ps} - 1.10875)^{0.23302}], \quad (21)$$

where u_{CB} is the CB velocity in km/s and t_{ps} is the time (ps) measured from the maximum of the laser pulse.

The RTI increment in a viscous liquid with allowance for surface tension (without regard for a finite atmosphere thickness) has the form [51]

$$\gamma = \sqrt{(2k^2\nu)^2 + gk\mathrm{At} - k^3\sigma/(\rho_{\mathrm{Au}} + \rho_{\mathrm{wt}})} - 2k^2\nu. \quad (22)$$

In Eq. (22), terms gk, At, $k^3\sigma/(\ldots)$, and $k^2\nu$ are related to buoyancy, capillarity, and viscosity, respectively. The density ratio is $\rho_{\mathrm{Au}}/\rho_{\mathrm{wt}} \approx 10$; therefore, the Atwood number is At ≈ 0.8 (see Appendix A). The wavenumber is $k = 2\pi/\lambda$. For waves $\lambda < h$, the atmosphere is considered to be thick, $kh > 6 > 1$.

Surface tension is approximated by the expression

$$\sigma(T) = \sigma_0\left(\frac{1 - T/T_{\mathrm{cr}}}{1 - T_m/T_{\mathrm{cr}}}\right)^{1.25}. \quad (23)$$

Here, we used the following parameters: $\sigma_0 = 1150$ dyn/cm, the critical temperature is $T_{\mathrm{cr}} = 7.8$ kK (see Fig. 4), the melting temperature of gold is $T_m = 1.338$ kK, and the surface tension of the gold melt at the melting point was borrowed from [76]. At near-critical temperatures, we have $\sigma = 155$, 84, and 25 dyn/cm at $T = 6.5$, 7.0, and 7.5 kK, respectively. The MD calculations of σ were described in [77]. Formula (23) was borrowed from [78] (also see Fig. 15 in [79]).

In Eq. (22), kinematic viscosity ν is taken to be the viscosity of gold (see Appendix B).

As is seen from Eq. (22), viscosity retards the growth of RTI but cannot stabilize CB. At any viscosity, the stabilization is determined by surface tension. CB becomes unstable at long modes, which are longer than the capillary scale

$$k_\sigma = \sqrt{\frac{\mathrm{At}\,g(\rho_{\mathrm{Au}} + \rho_{\mathrm{wt}})}{\sigma}}, \quad \lambda_\sigma[\mathrm{nm}] = \frac{21}{\sqrt{g_{14}}}.$$

In estimation, we take $\sigma = 100$ dyn/cm, At $= 0.8$, $\rho_{\mathrm{Au}} = 10$ g/cm^3, $\rho_{\mathrm{wt}} = 1$ g/cm^3, and $g = 10^{14} g_{14}$ cm/s^2 (also see Appendix A). Scale $\lambda_\sigma(g)$ is seen to increase with decreasing rate of deceleration $g(t)$ in time at fixed surface tension and densities (see Fig. 27). Thus, if wavelength λ is fixed, perturbation growth at this wavelength continues in a finite time interval to time t_*, when $g(t_*)$ decreases to $g = 10^{14}(21\ \mathrm{nm}/\lambda)^2$ (see Figs. 28–30). In other words, the growth of modes of larger scales continues for a longer time, and the increment of their growth is smaller.

Figures 28–30 show how RTI develops in terms of a linear theory. The parameters used for the calculation were as follows: $\sigma = 100$ dyn/cm, $\nu = 0.002$ cm^2/s (see Appendix B), $\rho_{\mathrm{Au}} = 10$ g/cm^3, and $\rho_{\mathrm{wt}} = 1$ g/cm^3. The deceleration was found from the expression, $g = du_{CB}/dt$, where $u_{CB}(t)$ is determined by Eq. (21). Figure 28 depicts the time dependence of instability increment γ according to Eq. (22). Figure 29 displays

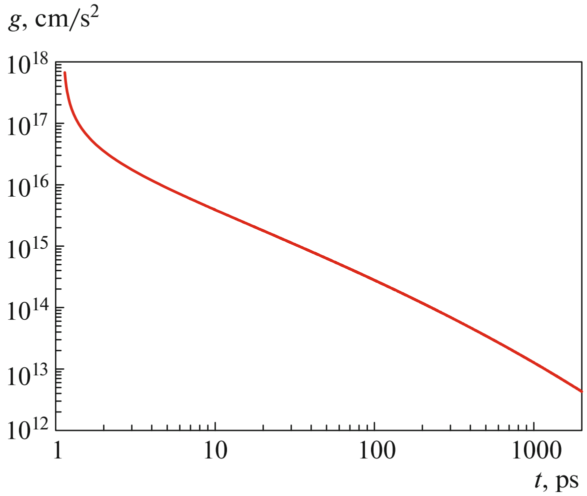

Fig. 27. (Color online) Deceleration of CB. It is brought about by water deceleration and the acceleration of the substance in the two-phase state by an accretion flux (see Figs. 2, 3, 17). Function $g(t)$ was obtained by the differentiation of the analytical approximation of velocity (21). Note that the accelerations of gold atoms under an interatomic interaction depend on temperature. These accelerations are about 10^{18} cm/s^2 in the case of the hot melt under study.

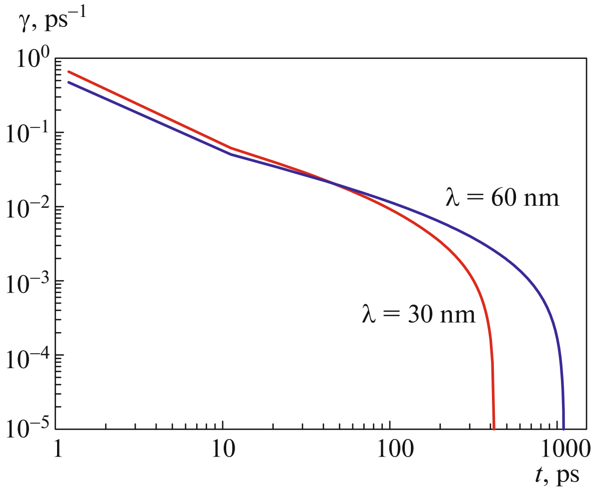

Fig. 28. (Color online) RTI increment (22). The amplitude grows in the time interval $0 < t < t_*$. At t_*, the mode is stabilized by surface tension (see text). The calculation parameters are $\sigma = 100$ dyn/cm and $\nu = 0.002$ cm^2/s.

how the value of $\int^t dt' g(t')$ is accumulated with time. Figure 30 illustrates the exponential amplification in the linear perturbation amplitude in the quasi-classical approximation, $a(t)/a(t_0) = \exp(\int^t \gamma(t')dt')$. The amplification is seen to be significant, by 1.5–2 orders of magnitude. Whether the perturbation extends to the nonlinear stage depends on the spectrum of initial perturbation amplitudes $a(t_0, \lambda)$. The $a(t_0, \lambda)$ perturbations are related to the initial target roughness, thermal fluctuations, and the bombardment of the outer atmosphere boundary by “nucleation products” (i.e., liquid fragments of two-phase mixture; see Fig. 3). An MD simulation is necessary to understand the development of the situation near the gold–water CB.

6. MD SIMULATION

We performed series of MD calculations. They differed in the width and the length of calculation parallelepiped $L_x \times L_y \times L_z$ and in initial data (absorbed energy F_{abs}). As above, axis x was directed along the main motion. The direct calculation of gold ablation to water requires huge computational resources. Even if we restrict ourselves to times of about 3 ns (rather than 200 ns, as in Section 5), the shock-compressed water layer thickness is about 10 μm, and SW reaches approximately the same depth in the gold volume in 3 ns. The transverse size should be at least several atmosphere thicknesses, i.e., $L_y = L_z > 100$ nm. This volume contains more than 10 billion atoms, and the number of integration steps to 3 ns at a step of about 1 fs is three millions.

Therefore, instead of the direct calculation, we developed a scheme with an equivalent physical approach and substantially smaller resources, namely, the number of atoms is smaller by two orders of magnitude. First, we sacrificed hydrodynamic three-dimensionality. The thickness of the calculation parallelepiped is $L_z = 8.2$ nm. As is known from the RTI theory, the two- and three-dimensional cases differ moderately from a quantitative standpoint [41, 42, 80]. Mix-

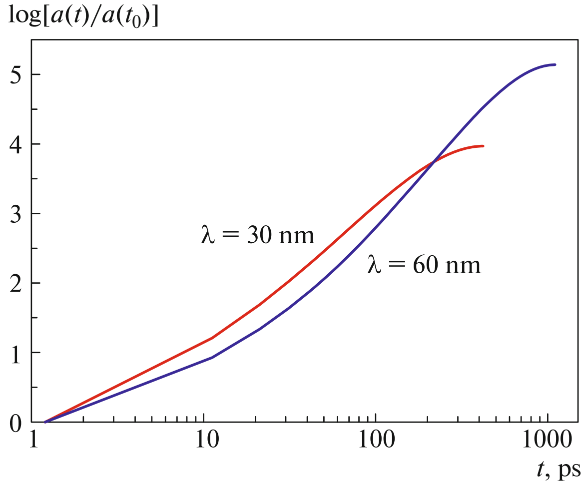

Fig. 29. (Color online) Increase in number $\int^t \gamma(t')dt'$ in time. Here, this number is called logarithmic accumulation.

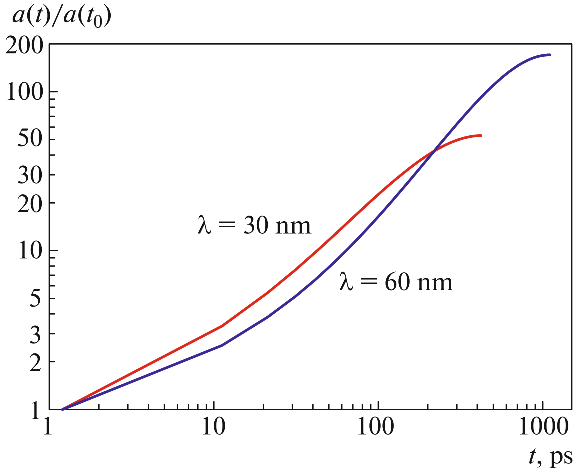

Fig. 30. (Color online) Amplification of perturbation amplitude $a(t) = a(t_0)\exp(\int^t \gamma(t')dt')$ by one–two orders of magnitude at the typical problem parameters.

ing coefficients α_+ are approximately the same and the rates of floating of bubbles are comparable [81].

Second, width L_y was varied: to check initial conditions, we first performed calculations at a relatively small width of 25 nm; then, we performed calculations at a width of 250 nm.

In addition, we used special-purpose techniques to cut "excess" water and "excess" gold. The point is that the length of the layer involved in motion, $L_{\text{total}} = L_{\text{Au}} + L_{\text{wt}}$ (along x), is large because of the running of a compression wave in gold and SW in water from the initial CB plane. These waves move at the velocities loops that are close to the velocity of sound or even exceed it. The velocity of sound is very high as compared to the velocities of motion in the much thinner (as compared to L_{total}) contact layer near CB. CB velocity $u_{CB}(t)$ is on the order of c_s only at the acoustic stage of time $t_s = d_T/c_s$ (see Fig. 26).

After the end of the stage of nucleation, the compression wave in gold and the near-contact region are separated by the two-phase layer, which is under near-zero pressures and has a low velocity of sound. The events that occur in the compression wave in gold (its propagation, breaking, elastoplastic splitting [60]) do not affect the near-contact layer. The nucleation time is on the order of t_s. Nucleation continues until the rarefaction wave leaves the laser heating layer of thickness d_T after the compression wave in gold. Therefore, we chose time t_{crop}, when the thick two-phase layer is cut by the plane, on the times of several scales of t_s. The gold atoms located at the depths behind this plane are not involved in the simulation at $t > t_{\text{crop}}$. A similar technique is used to decrease the number of Lagrangian cells in the 2*T*HD code. The clipping of excess gold was illustrated in Fig. 19.

As was noted in Section 3, a region at rest with a zero pressure is retained behind the pair of waves coming to the gold volume. Therefore, gold can easily be cut off. The situation with clipping excess water is more complex.

After choosing the required initial conditions (i.e., proper heating conditions), we performed calculation to 400 ps at a narrow width (L_y = 25 nm). We sought for the trajectory $x_{140}(t)$ of a Lagrangian particle (material particle), which was located at a distance of 140 nm from CB before laser heating. After time t = 400 ps, function $x_{140}(t)$ was smoothly analytically continued to t = 1 ns. What is the Lagrangian particle in an MD calculation? We chose a group of neighboring water molecules at a distance of 140 nm from the initial position of CB and wrote the trajectory of their center of mass. This trajectory was function $x_{140}(t)$.

Instead of the calculation with a thick water layer, we perform an MD calculation with a thinner water layer located in the gap between CB and boundary $x_{140}(t)$. In the case of "thick" water, SW exists in water up to t = 400 ps. A comparison of thick-water calculation A with a full layer of shock-compressed water and calculation B limited by boundary $x_{140}(t)$ demonstrates that they are almost equivalent. In calculation B, the water layer boundary was subjected to forced motion according to law $x_{140}(t)$.

The clipping of excess water was combined with a tenfold increase in width L_y from 25 to 250 nm. Width L_y is very important for a successful simulation of the development of RTI, which is strongly retarded in narrow channels. The large-width calculation is called B-multi.

The tenfold increase in width L_y from 25 to 250 nm consists in the fact that calculation B at time t_{multi} is multiplied into ten bands (or channels), which are joined into one channel. At $t > t_{\text{multi}}$, the B-multi calculation is performed in a calculation parallelepiped with L_y = 250 nm. Calculations B and B-multi are nonequivalent because of another arrangement of Voronoi cells in calculation B-multi as compared to calculation B. RTI rapidly enhances this nonequivalence. As a result, the wide B-multi channel does operates as a wide channel from the very beginning of laser heating. Thus, we conduct a calculation with large width L_y and a much smaller number of water molecules as compared to direct simulation.

For the important stage of CB deceleration not to be omitted, the B-multi calculation begins with time t_{start} on the order of the time to the onset of nucleation. All stages of CB deceleration are substantial for RTI accumulation and amplification via the RTI mechanism (see Figs. 28–30).

Figure 31 shows the results of calculations A, B, and B-multi. The horizontal frame size is L_y = 249.2 nm, the pixel size is 0.623 nm, and the upper boundary of the frames in Fig. 31 is Lagrangian parti-

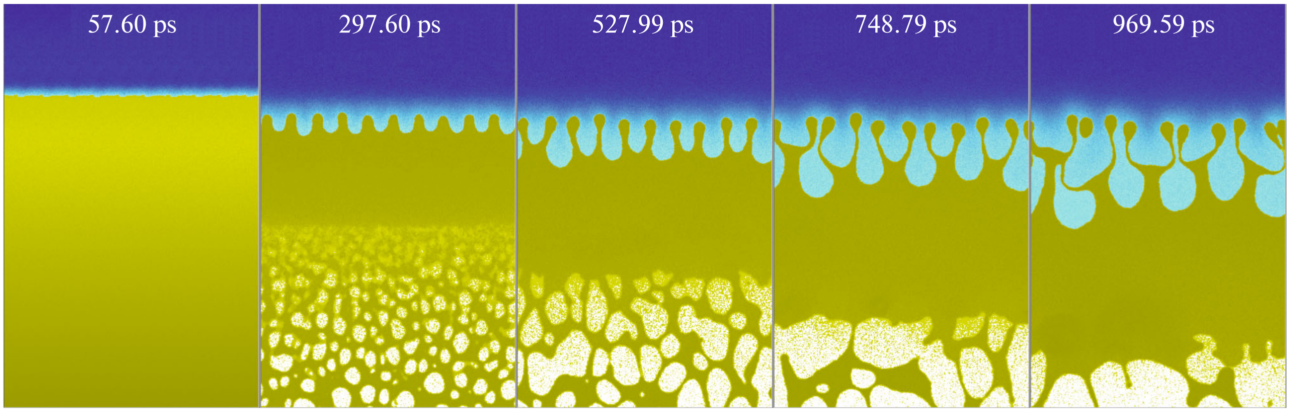

Fig. 31. (Color online) Amplification of Rayleigh–Taylor perturbations because of the deceleration of atmosphere by the water pressure. Gold is yellow water is blue. Water changes its color from dark blue to light blue because of strong heating near the gold–water boundary. A separated gold droplet is visible in the last frame. This is one of the mechanisms of nanoparticle formation during ablation into liquid.

cle $x_{140}(t)$. After SW goes out of boundary $x_{140}(t)$ in water, the water layer thickness increases slowly because of a constant decrease in the pressure in the near-contact layer (see the $p_{CB}(t)$ curve in Fig. 24). A decrease in the pressure decreases the water density, and this effect is numerically moderate. Correspondingly, the thickness of the water layer shown in Fig. 31 (region occupied by water is blue) also increases. The effect of decreasing the degree of water compression and the expansion of the layer bounded by surface $x_{140}(t)$ is combined with the strong deformation of the water–gold CB because of the development of RTI and with the strong heating of water near CB (hot water expands additionally). The total number of atoms in the calculation presented in Fig. 31 is about 50 millions.

The atmosphere boundary accretion of the two-phase mixture of melt fragments and vapor-filled cavities is clear in Fig. 31 (cf. with Figs. 2, 3, 15–18). The atmosphere in Fig. 31 is represented by a continuous single-phase gold layer. The pressure in it grows from bottom to top. Because of accretion, the atmosphere thickness in Fig. 31 increases in time despite the increase in the gold density in the atmosphere due its gradual cooling, which is caused by heating of water and heat transfer through foam membranes and filaments to the foam body (where the foamed gold temperature is lower than in the hot atmosphere). In water, it has low but substantial atomic heat conduction. The electronic heat conduction in gold is much higher. It is simulated by the Monte Carlo unit embedded into the MD algorithm with dynamic decomposition along Voronoi polyhedra [82].

It is now unclear how the noise of the splashes of liquid-fragment impacts on the boundary between the atmosphere and the two-phase mixture influences the development of RTI. The influence of the impact of a fragment of length λ along y decays exponentially across the atmosphere thickness at a depth $1/k = \lambda/2\pi$, or $k = 2\pi/\lambda$. First, impact velocity Δu is low (see Figs. 17, 18); however, the rate of RTI development is low. Second, depth $\lambda/2\pi$ is smaller than the current atmosphere thickness. $\lambda(t)$, i.e., the foam cell size, increases in time and the atmosphere thickness increases.

Based on similar considerations (regarding decay at depth $\lambda/2\pi$), we chose a water layer thickness of 140 nm, which determines function $x_{140}(t)$. The growth of the RTI modes with the scale along axis y shown in Fig. 31 does not affect surface $x = x_{140}(t)$. Correspondingly, boundary $x = x_{140}(t)$ made of Lagrangian water particles remains flat (horizontal in Fig. 31) despite the very strong deformation of CB.

Figures 32–34 show the profile evolution corresponding to the calculation in Fig. 31.

7. CONCLUSIONS

We considered the ablation of the gold surface into water under a femtosecond laser pulse, the energy of which is absorbed in the skin layer of gold after passage through transparent water. The results of two-temperature one-dimensional hydrodynamic calculations of the expansion of the strongly heated surface layer of the gold melt into water were presented. The expansion leads to the nucleation of vapor cavities in the melt. As a result, the layer of a two-phase mixture of the liquid and vapor phases of gold appears. The water deceleration of the expansion of gold causes the formation of a contact gold layer, where the two-phase mixture returns to the single-phase state. The single-phase contact layer of gold is in contact with water, through which SW moves. The deceleration in the noninertial coordinate system related to the contact is equivalent to the action of gravitational field. Thus, the high-density gold melt is in the state where the

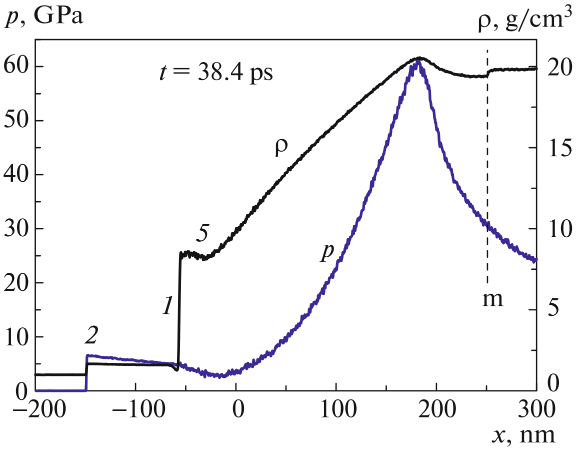

Fig. 32. (Color online) Pressure and density profiles in the MD simulation of version A: narrow channel $L_y = 25$ nm without cutting the part of foam adjacent to the crater bottom and without boundary $x_{140}(t)$. The results are similar to those presented in Section 5: (*2*) SW in water, (*1*) CB, and (*5*) upper atmosphere boundary (cf. with Figs. 2, 3).

melt is supported in the gravitational field by the pressure of the low-density liquid. Such states are known to be unstable. The contact boundary between gold and water is strongly deformed because of the development of RTI. The results of a large-scale MD simulation of gold ablation into water are presented, and they fully support the possibility of RTI development. This instability leads to the formation of capillary-scale gold nanoparticles during the fragmentation of liquid gold jets.

APPENDIX A

BOUNDARY DECELERATION: SPALLATION AND INSTABILITY

The decay of pressure discontinuity at the contact of two homogeneous half-spaces differs qualitatively from the decay in the presence of inhomogeneity. In the former case, the flow is self-similar (see Section 2), the self-similar coordinate is x/t, CB moves toward the low-pressure medium at a constant velocity, and the CB deceleration is zero ($g = 0$; see Fig. 6). In the calculation of self-similar coordinate x/t, time t is measured from the decay of discontinuity. In the second case, CB decelerates ($g \neq 0$; see Section 3 about the cause of deceleration). According to the Einstein equivalence principle (lift effect), a gravitational field appears in the noninertial coordinate system related to CB. This is the qualitative difference between the former and latter cases.

Deceleration g consists of the tension resistance of the condensed phase g_{intrn} and the deceleration by an external inertial medium g_{extrn}. We now analyze expansion into vacuum. In this case, the deceleration by cohesion forces is only retained. In the simplest model, we have a horizontal liquid layer in the gravitational field at the ceiling. Let liquid atoms be cohesively strongly connected with fixed ceiling atoms. The pressure is zero at CB with vacuum. In hydrostatic equilibrium, we have $p = -\rho|g|x$; that is, the pressure decreases linearly into the liquid volume. We assumed $x = 0$ at CB, and the extension-induced decrease in the density of the condensed phase can easily be introduced into a hydrostatic equation (this change is neglected here).

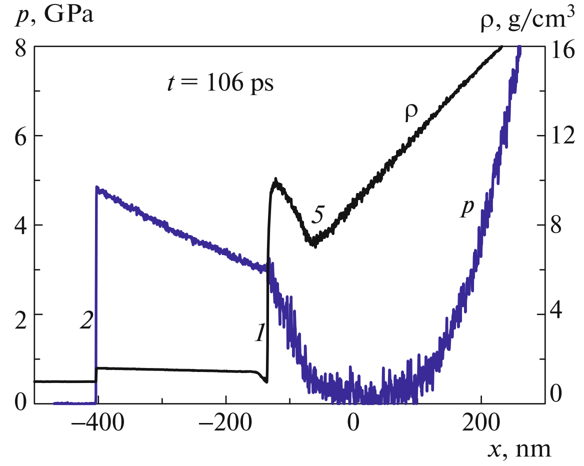

Fig. 33. (Color online) Near-contact region. Stage when a compression wave went to the right. The pressure drop at the atmosphere is related to the gold layer weight in the water-decelerated atmosphere.

The increase in RTI is maximal in the absence of stabilization by surface tension and viscosity. An inverse scaling cascade creates an ensemble of bubbles

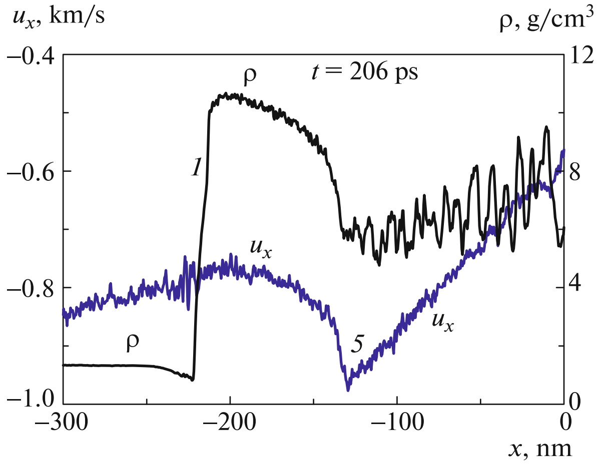

Fig. 34. (Color online) Velocity jump down (deceleration) at the upper atmosphere boundary, where the two-phase mixture enters the atmosphere (cf. with the analogous behavior in the 2*T*HD calculation with velocity jump Δu in Figs. 14, 17, 18).

moving up along the liquid layer [41, 42, 80, 83]. The approximate layer thickness in which pressure increases from negative to zero vacuum pressure due to the lifting of bubbles is

$$h_+ = \alpha_+ \mathrm{At} g t^2, \quad \mathrm{At} = \frac{\rho_2 - \rho_1}{\rho_2 + \rho_1},$$

where time t is measured from the creation of the initially immobile suspended layer, thickness h_+ is measured from the initial CB plane ($x = 0$), and the Atwood number is $\mathrm{At} = 1$ in the case of vacuum.

The growth time of the fragmentation layer of continuous liquid $h_+ = \alpha_+ g t^2$ is limited by the time of CB deceleration. The deceleration time for fluences from $F_{\mathrm{abs}} = 0$ to the nucleation threshold is determined by the time of reflection of the acoustic compression wave moving to CB from CB (see Section 3). This time is on the order of the acoustic time scale $t_s = d_T/c_s$. Therefore, the maximum fragmented liquid thickness is

$$h_{\max} = \alpha_+ g t_s^2 \sim \alpha_+ u t_s \approx \alpha_+ (p/Z) t_s,$$
$$h_{\max} \sim \alpha_+ (u/c_s) d_T,$$

where $g \sim u/t_s$ and $u \approx p/Z$. Quantity $\alpha_+ \approx 0.03$–0.05 is well below unity [41, 42, 80, 83]. Note that this quantity weakly depends on the variation of the Atwood number ($\mathrm{At} \in [0, 1]$) and the space dimension (2D–3D) despite the fact that the cases with $\mathrm{At} = 1$ or 2D geometry differ radically from the situation 3D, $\mathrm{At} < 1$ by the absence of the Kolmogorov dissipation in the case with $\mathrm{At} = 0$ or in the case with 2D geometry.

Velocity u and Mach number u/c_s increase with absorbed energy F_{abs}, since $u \approx p/Z$ and $p \sim F_{\mathrm{abs}}/d_T$. This increase continues up to the nucleation threshold. This threshold is slightly lower than the spallation threshold: the difference is from several units to several tens of percent [25, 26, 84]. We neglect this difference in our estimation. At the nucleation threshold, p in the acoustic estimation $u \approx p/Z$ is approximately equal to the ultimate tensile strength of a substance p_{strng}. In ultrashort pulse experiments, strength p_{strng} is substantially higher (by an order of magnitude) than the strength on large space–time scales. However, the Mach number is small (several percent) even in the situation with ultrashort pulses, $u_{\mathrm{nucl}}/c_s \approx p/Z/c_s \approx p_{\mathrm{strng}}/B$, where B is the bulk modulus. In the case of large scales (e.g., $d_T \sim 1$ mm, $t_s \sim 10^{-6}$ s), ratio u_{nucl}/c_s is lower by another order of magnitude.

Thus, the ratio $h_{\max}/d_T \sim \alpha_+(u/c_s) \sim 10^{-4}$ is very low. Moreover, for perturbations with harmonic sizes $\langle\lambda\rangle \sim h_+$ to appear, average length $\langle\lambda\rangle$ should exceed the capillary and viscosity scales:

$$\lambda_\sigma = 2\pi\sqrt{\sigma/g/\rho}$$
$$= 80\left(\frac{\sigma}{300\,\mathrm{dyn/cm}} \Big/ \frac{g}{10^{13}\ \mathrm{cm/s^2}} \Big/ \frac{\rho}{19.3\ \mathrm{g/cm^3}}\right)^{1/2}\ \mathrm{nm},$$

$$\lambda_\nu = 2\pi(\nu^2/\mathrm{At}/g)^{1/3}$$
$$= 40\left(\frac{\nu}{0.0015\ \mathrm{cm^2/s}}\right)^{2/3} \Big/ \left(\frac{g}{10^{13}\ \mathrm{cm/s^2}}\right)^{1/3}\ \mathrm{nm},$$

where ν is the kinematic viscosity of gold (see Appendix B), which is obtained from dynamic viscosity by division by density ρ. In the estimates, we assumed $\mathrm{At} = 1$. Viscosity length λ_ν is found from the condition $\mathrm{Re} = v_\nu k_\nu^{-1}/\nu = 1$, where Re is the Reynolds number, $v_\nu = \sqrt{\mathrm{At}\, g\, k_\nu^{-1}}$, and $\lambda_\nu = 2\pi/k_\nu$.

As is seen from these formulas, the RTI effects are weak in the case of an ultrashort pulse and the expansion of the surface nanolayer of a bulk target into vacuum. Indeed, we have a low ratio $h_{\max}/d_T \sim 10^{-4}$; $h_{\max}$ cannot be detected at $d_T \sim 100$ nm. In addition, we have capillarity and viscosity limitations.

To complete the picture, we analyze whether RTI can be detected at very large thicknesses ($d_T \sim 100$ cm). Then, we have $h_{\max} \sim 100$ μm, $t_s \sim 300$ μs, and $g \approx 3 \times 10^7$ cm/s^2 if $\Delta u \sim 100$ m/s (here, Δu is the decrease in the CB velocity in the temporal segment of CB deceleration by cohesion forces). An increase in d_T is seen to decrease deceleration g strongly. Correspondingly, the capillary (up to 50 μm) and viscosity (up to 3 μm) scales grow. The capillary scale is comparable with $h_{\max}$, so that RTI is low-scale and weak.

Note that, above the nucleation and spallation thresholds, velocity Δu rather than CB velocity u at the decay of discontinuity should be substituted into the formulas given above. The point is that CB does not stop under cohesion forces above the spallation threshold. u increases and Δu decreases with increasing ratio $F_{\mathrm{abs}}/F_{\mathrm{abs|abl}}$. The ratio $F_{\mathrm{abs}}/F_{\mathrm{abs|abl}}$ characterizes the superthreshold. In the "hot" situation with a high superthreshold (ratio of 3–5), both the deceleration and the decrease in the velocity become low.

In conclusion of this Appendix, we note that cohesion forces cause both RTI and spallation effects. Thus, these phenomena are related through deceleration and noninertia. Both phenomena cause ruptures and fragmentation. Spallation is caused by the limitation of resistance to stretching by a finite strength. Note that a similar situation (weak RTI) appears during spallation when SW of thickness d_T reaches the free surface in liquid. In the case of an initially cold solid metal, the spallation threshold is usually lower than the melting threshold in SW. If the SW amplitude reaches the melting threshold, the cohesion-induced decrease in the velocity (Δu) is usually small.

In this Appendix, we consider the case where CB deceleration is completely caused by the cohesion of the condensed phase. In this article devoted to gold ablation into water, we focus on the situation where, first, cohesion is weak because of high superthreshold $F_{\mathrm{abs}}/F_{\mathrm{abs|abl}}$. Correspondingly, gold is heated to near- or

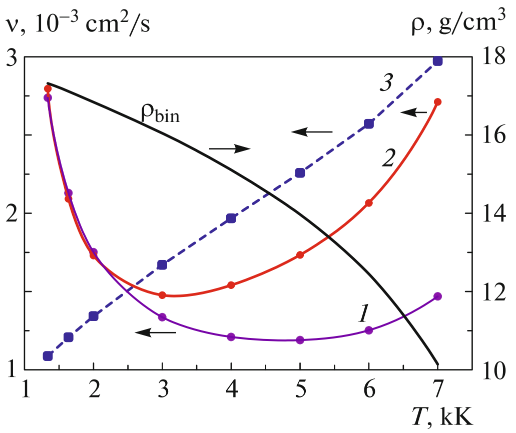

Fig. 35. (Color online) Kinematic viscosity ν of gold over a wide temperature range from the melting temperature to the vicinity of the critical point. Curve ρ of the thermal expansion of the gold melt was calculated using the data from [46–48].

supercritical temperatures and the surface tension becomes very low or disappears. Second, deceleration occurs due to the inertia of the environment, namely, water. The deceleration layer (atmosphere) is fed by the flux of the nondecelerated substance flying in a rarefaction wave (see Figs. 2, 3). Feeding with mass and momentum takes place.

In the text body, we noted the similarity between this problem and the problems of astrophysics (magnetosphere instability, expansion of supernova remnant) [38–43] and explosion physics (see Section 1) [44, 45]. Note that the geometry of expansion substantially affects the mixing intensity. The development of RTI is slowest in 1D geometry. Above, we considered the problem of gold ablation into water in the 1D case, where heating spot diameter $2R_L$ is large (several hundred microns). The dynamics of destruction of the atmospheric shell and the formation of nanoparticles in water can be controlled by decreasing diameter $2R_L$ to several tens or several microns. This problem needs a separate consideration. The problem of substance expansion into vacuum from small heating spots has recently been comprehensively studied in [85, 86].

APPENDIX B

VISCOSITY OF HOT GOLD

Figure 35 shows the experimental data on the viscosity of gold in a binodal. The MD calculations of the viscosity in the binodal and outside it (i.e., at high pressure) needs a separate investigation. Curves *1* and *2* in Fig. 35 are the far extrapolation of the approximation formulas from [87], where the viscosities at the first two points (T = 1.336 and 1.637 kK) on the left in curves *1* and *2* were measured. We also used data for the density of the liquid phase in the binodal of gold from [46–48].

We first calculate the dynamic viscosity in poise using the formulas from [87],

$$\eta[\mathrm{P}] = 0.01133\exp(1.91/T[\mathrm{kK}]).$$

The obtained values are divided by the gold density in the binodal $\rho_{\mathrm{bin}}(T)$, and the kinematic viscosity $\nu = \eta/\rho$ shown in curve *1* in Fig. 35 is obtained. In the case of curve *2*, the formula for η is

$$\eta[\mathrm{P}] = 0.00232T[\mathrm{kK}]\exp(3.67/T[\mathrm{kK}]).$$

Curve *3* gives the viscosity estimated by a molecular–kinetic theory,

$$\nu = u_T l, \quad u_T = \sqrt{\frac{3k_{\mathrm{B}}T}{M}}, \quad l = n^{-1/3},$$

where u_T is the thermal velocity, M is the gold atom mass, and n is the concentration of gold atoms in the melt in the binodal.

ACKNOWLEDGMENTS

This work was supported by the Russian Science Foundation, project no. 14-19-01599.

REFERENCES

1. C.-K. Sun, F. Vallee, L. H. Acioli, E. P. Ippen, and J. G. Fujimoto, Phys. Rev. B **50**, 15337 (1994).
2. X. Y. Wang, D. M. Riffe, Y. S. Lee, and M. C. Downer, Phys. Rev. B **50**, 8016 (1994).
3. J. Hohlfeld, S.-S. Wellershoff, J. Guedde, U. Conrad, V. Jaehnke, and E. Matthias, Chem. Phys. **251**, 237 (2000).
4. D. Strickland and G. Mourou, Opt. Commun. **55**, 447 (1985).
5. M. Pessot, P. Maine, and G. Mourou, Opt. Commun. **62**, 419 (1987).
6. K. Phillips, H. Gandhi, E. Mazur, and S. Sundaram, Adv. Opt. Photon. **7**, 684 (2015).
7. M. C. Downer, R. L. Fork, and C. V. Shank, J. Opt. Soc. Am. B **4**, 595 (1985).
8. V. V. Temnov, K. Sokolowski-Tinten, P. Zhou, and D. von der Linde, J. Opt. Soc. Am. B **23**, 1954 (2006).
9. S. I. Anisimov, B. L. Kapeliovich, and T. L. Perel'man, Sov. Phys. JETP **39**, 375 (1974)].
10. N. A. Inogamov, V. V. Zhakhovskii, S. I. Ashitkov, V. A. Khokhlov, V. V. Shepelev, P. S. Komarov, A. V. Ovchinnikov, D. S. Sitnikov, Yu. V. Petrov, M. B. Agranat, S. I. Anisimov, and V. E. Fortov, Contrib. Plasma Phys. **51**, 367 (2011).
11. K. Sokolowski-Tinten, J. Bialkowski, A. Cavalleri, et al., Phys. Rev. Lett. **81**, 224 (1998).
12. N. A. Inogamov, A. M. Oparin, Yu. V. Petrov, N. V. Shaposhnikov, S. I. Anisimov, D. von der Linde, and J. Meyer-ter-Vehn, JETP Lett. **69**, 310 (1999).
13. V. V. Zhakhovskii, K. Nishikhara, S. I. Anisimov, and N. A. Inogamov, JETP Lett. **71**, 167 (2000).

14. L. V. Zhigilei and B. J. Garrison, J. Appl. Phys. **88**, 1281 (2000).
15. B. J. Demaske, V. V. Zhakhovsky, N. A. Inogamov, and I. I. Oleynik, Phys. Rev. B **82**, 064113 (2010).
16. D. S. Ivanov and L. V. Zhigilei, Phys. Rev. B **68**, 064114 (2003).
17. M. Gill-Comeau and L. J. Lewis, Phys. Rev. B **84**, 224110 (2011).
18. Yu. V. Petrov, N. A. Inogamov, and K. P. Migdal, JETP Lett. **97**, 20 (2013).
19. Yu. V. Petrov, K. P. Migdal, N. A. Inogamov, and S. I. Anisimov, JETP Lett. **104**, 431 (2016).
20. P. Lorazo, L. J. Lewis, and M. Meunier, Phys. Rev. B **73**, 134108 (2006).
21. C. Wu, M. S. Christensen, J.-M. Savolainen, P. Balling, and L. V. Zhigilei, Phys. Rev. B **91**, 035413 (2015).
22. P. N. Mayer and A. E. Mayer, J. Appl. Phys. **120**, 075901 (2016).
23. E. T. Karim, M. V. Shugaev, Chengping Wu, Zhibin Lin, H. Matsumoto, M. Conneran, J. Kleinert, R. F. Hainsey, and L. V. Zhigilei, Appl. Phys. A **122**, 407 (2016).
24. Chengping Wu and L. V. Zhigilei, J. Phys. Chem. C **120**, 4438 (2016).
25. V. V. Zhakhovskii, N. A. Inogamov, and K. Nishihara, JETP Lett. **87**, 423 (2008).
26. V. Zhakhovskii, N. Inogamov, and K. Nishihara, J. Phys.: Conf. Ser. **112**, 042080 (2008).
27. N. A. Inogamov, V. V. Zhakhovskii, S. I. Ashitkov, Yu. V. Petrov, M. B. Agranat, S. I. Anisimov, K. Nishikhara, and V. E. Fortov, J. Exp. Theor. Phys. **107**, 1 (2008).
28. N. A. Inogamov, V. V. Zhakhovsky, V. A. Khokhlov, S. I. Ashitkov, Yu. N. Emirov, K. V. Khichshenko, A. Ya. Faenov, T. A. Pikuz, M. Ishino, M. Kando, N. Hasegawa, M. Nishikino, P. S. Komarov, B. J. Demaske, M. B. Agranat, et al., J. Phys.: Conf. Ser. **510**, 012041 (2014).
29. N. A. Inogamov, V. V. Zhakhovsky, S. I. Ashitkov, Yu. N. Emirov, A. Ya. Faenov, T. A. Pikuz, M. Ishino, M. Kando, N. Hasegawa, M. Nishikino, T. Kawachi, M. B. Agranat, A. V. Andriash, S. E. Kuratov, and I. I. Oleynik, J. Phys.: Conf. Ser. **500**, 112070 (2014).
30. N. A. Inogamov, V. V. Zhakhovsky, N. Hasegawa, M. Nishikino, M. Yamagiwa, M. Ishino, M. B. Agranat, S. I. Ashitkov, A. Ya. Faenov, V. A. Khokhlov, D. K. Ilnitsky, Yu. V. Petrov, K. P. Migdal, T. A. Pikuz, S. Takayoshi, et al., Appl. Phys. B **119**, 413 (2015).
31. N. A. Inogamov, V. V. Zhakhovsky, and V. A. Khokhlov, in *Proceedings of the Progress in Electromagnetics Research Symposium PIERS, Prague, Czech Republic, July 6—9, 2015*, p. 2413.
32. S. I. Ashitkov, S. A. Romashevskii, P. S. Komarov, A. A. Burmistrov, V. V. Zhakhovsky, N. A. Inogamov, and M. B. Agranat, Quantum Electron. **45**, 547 (2015).
33. A. Y. Vorobyev and Chunlei Guo, Opt. Express **14**, 2164 (2006).
34. A. A. Ionin, S. I. Kudryashov, S. V. Makarov, A. O. Levchenko, A. A. Rudenko, I. N. Saraeva, D. A. Zayarny, Ch. R. Nature ala, and W. Husinsky, Laser Phys. Lett. **13**, 025603 (2016).
35. M. B. Agranat, S. I. Anisimov, S. I. Ashitkov, V. V. Zhakhovskii, N. A. Inogamov, K. Nishihara, A. M. Oparin, Yu. V. Petrov, V. E. Fortov, and V. A. Khokhlov, Appl. Surf. Sci. **253**, 6276 (2007).
36. S. I. Anisimov, V. V. Zhakhovskii, N. A. Inogamov, K. Nishikhara, Yu. V. Petrov, and V. A. Khokhlov, J. Exp. Theor. Phys. **103**, 183 (2006).
37. S. G. Bezhanov, A. P. Kanavin, and S. A. Uryupin, Quantum Electron. **46**, 119 (2016).
38. N. R. Sibgatullin, *Oscillations and Waves in Strong Gravitation and Electromagnetic Fields* (Nauka, Moscow, 1984).
39. J. Arons and S. M. Lea, Astrophys. J. **207**, 914 (1976).
40. N. A. Inogamov and R. A. Sunyaev, Astron. Lett. **25**, 269 (1999); Astron. Lett. **36**, 835 (2010).
41. N. A. Inogamov, A. Yu. Dem'yanov, and E. E. Son, *Hydrodynamics of Mixing: Periodic Structures, Amplification of Subharmonics, Inversion Cascade* (Mosk. Fiz. Tekh. Inst., Moscow, 1999) [in Russian].
42. N. A. Inogamov, Astrophys. Space Phys. Rev. **10**, 1 (1999).
43. F. Fraschetti, R. Teyssier, J. Ballet, and A. Decourchelle, Astron. Astrophys. **515**, A104 (2010).
44. S. I. Anisimov, Y. B. Zeldovich, N. A. Inogamov, and M. F. Ivanov, Progr. Astronaut. Aeronaut. **87**, 218 (1983).
45. K. Balakrishnan, F. Genin, D. V. Nance, and S. Menon, Shock Waves **20**, 147 (2010).
46. A. V. Bushman, V. E. Fortov, G. I. Kanel, and A. L. Ni, *Intense Dynamic Loading of Condensed Matter* (Taylor and Francis, London, New York, 1993).
47. K. V. Khishchenko, S. I. Tkachenko, P. R. Levashov, I. V. Lomonosov, and V. S. Vorobev, Int. J. Thermophys. **23**, 1359 (2002).
48. http://teos.ficp.ac.ru/rusbank/. http://www.ihed.ras.ru/rusbank/.
49. https://en.wikipedia.org/wiki/Gold.
50. S. Chandrasekhar, *Hydrodynamic and Hydromagnetic Stability* (Oxford Univ. Press, London, 1968).
51. K. O. Mikaelian, Phys. Rev. E **54**, 3676 (1996).
52. G. E. Norman, S. V. Starikov, and V. V. Stegailov, J. Exp. Theor. Phys. **114**, 792 (2012).
53. N. A. Inogamov, S. I. Anisimov, and B. Retfel'd, J. Exp. Theor. Phys. **88**, 1143 (1999).
54. S. I. Anisimov, N. A. Inogamov, and A. M. Oparin, Izv. Akad. Nauk, Ser. Mekh. Zhidk. Gaza **34** (6), 149 (1999).
55. S. I. Anisimov, N. A. Inogamov, A. M. Oparin, B. Rethfeld, T. Yabe, M. Ogawa, and V. E. Fortov, Appl. Phys. A **69**, 617 (1999).
56. B. Chimier and V. T. Tikhonchuk, Phys. Rev. B **79**, 184107 (2009).
57. R. I. Nigmatulin and R. Kh. Bolotnova, High Temp. **49**, 303 (2011).
58. V. V. Zhakhovskii, N. A. Inogamov, Yu. V. Petrov, S. I. Ashitkov, and K. Nishihara, Appl. Surf. Sci. **255**, 9592 (2009).
59. M. E. Povarnitsyn, V. B. Fokin, and P. R. Levashov, Appl. Surf. Sci. **357**, 1150 (2015).

60. B. J. Demaske, V. V. Zhakhovsky, N. A. Inogamov, and I. I. Oleynik, Phys. Rev. B **87**, 054109 (2013).
61. M. E. Povarnitsyn, T. E. Itina, P. R. Levashov, and K. V. Khishchenko, Phys. Chem. Chem. Phys. **15**, 3108 (2013).
62. M. E. Povarnitsyn and T. E. Itina, Appl. Phys. A **117**, 175 (2014).
63. T. E. Itina, J. Phys. Chem. C **115**, 5044 (2011).
64. Cheng-Yu Shih, Chengping Wu, M. V. Shugaev, and L. V. Zhigilei, J. Colloid Interface Sci. **489**, 3 (2017).
65. N. A. Inogamov, Yu. V. Petrov, V. V. Zhakhovsky, V. A. Khokhlov, B. J. Demaske, S. I. Ashitkov, K. V. Khishchenko, K. P. Migdal, M. B. Agranat, S. I. Anisimov, V. E. Fortov, and I. I. Oleynik, AIP Conf. Proc. **1464**, 593 (2012).
66. M. E. Povarnitsyn, T. E. Itina, M. Sentis, P. R. Levashov, and K. V. Khishchenko, Phys. Rev. B **75**, 235414 (2007).
67. Yu. Petrov, K. Migdal, N. Inogamov, and V. Zhakhovsky, Appl. Phys. B **119**, 401 (2015).
68. Yu. V. Petrov and N. A. Inogamov, JETP Lett. **98**, 278 (2013).
69. K. P. Migdal, Yu. V. Petrov, and N. A. Inogamov, Proc. SPIE **9065**, 906503 (2013).
70. K. Migdal, Yu. Petrov, D. Il'nitsky, V. Zhakhovsky, N. Inogamov, K. Khishchenko, D. Knyazev, and P. Levashov, Appl. Phys. A **122**, 408 (2016).
71. D. K. Ilnitsky, V. A. Khokhlov, V. V. Zhakhovsky, Yu. V. Petrov, K. P. Migdal, and N. A. Inogamov, J. Phys.: Conf. Ser. **774**, 012101 (2016).
72. Zh. Lin, L. V. Zhigilei, and V. Celli, Phys. Rev. B **77**, 075133 (2008).
73. A. Ng, Int. J. Quantum Chem. **112**, 150 (2012).
74. N. A. Inogamov, V. V. Zhakhovskii, S. I. Ashitkov, V. A. Khokhlov, Yu. V. Petrov, P. S. Komarov, M. B. Agranat, S. I. Anisimov, and K. Nishihara, Appl. Surf. Sci. **255**, 9712 (2009).
75. L. D. Landau and E. M. Lifshitz, *Course of Theoretical Physics*, Vol. 6: *Fluid Mechanics* (Nauka, Moscow, 1986; Pergamon, New York, 1987).
76. E. B. Webb III and G. S. Grest, Phys. Rev. Lett. **86**, 2066 (2001).
77. S. I. Anisimov, D. O. Dunikov, V. V. Zhakhovskii, and S. P. Malyshenko, J. Chem. Phys. **110**, 8722 (1999).
78. V. K. Semenchenko, *Surface Phenomena in Metals and Alloys* (Pergamon, New York, 1961).
79. N. A. Inogamov, V. V. Zhakhovskii, and V. A. Khokhlov, J. Exp. Theor. Phys. **120**, 15 (2015).
80. N. A. Inogamov, A. M. Oparin, A. Yu. Dem'yanov, L. N. Dembitski, and V. A. Khokhlov, J. Exp. Theor. Phys. **92**, 715 (2001).
81. N. A. Inogamov and A. M. Oparin, J. Exp. Theor. Phys. **89**, 481 (1999).
82. V. Zhakhovskii, K. Nishihara, Y. Fukuda, S. Shimojo, T. Akiyama, S. Miyanaga, H. Sone, H. Kobayashi, E. Ito, Y. Seo, M. Tamura, and Y. Ueshima, in *IEEE Proceedings of the 5th International Symposium on Cluster Computing and Grid CCGrid 2005, May 9-12, 2005, Cardiff, UK* (2005), Vol. 2, p. 848.
83. G. Dimonte, D. L. Youngs, A. Dimits, S. Weber, M. Marinak, S. Wunsch, C. Garasi, A. Robinson, M. J. Andrews, P. Ramaprabhu, A. C. Calder, B. Fryxell, J. Biello, L. Dursi, P. MacNeice, K. Olson, P. Ricker, R. Rosner, F. Timmes, H. Tufo, Y.-N. Young, and M. Zingale, Phys. Fluids **16**, 1668 (2004).
84. S. I. Ashitkov, N. A. Inogamov, V. V. Zhakhovskii, Yu. N. Emirov, M. B. Agranat, I. I. Oleinik, S. I. Anisimov, and V. E. Fortov, JETP Lett. **95**, 176 (2012).
85. N. A. Inogamov, V. V. Zhakhovsky, V. A. Khokhlov, Yu. V. Petrov, and K. P. Migdal, Nanoscale Res. Lett. **11**, 177 (2016).
86. P. A. Danilov, D. A. Zayarny, A. A. Ionin, S. I. Kudryashov, A. A. Rudenko, A. A. Kuchmizhak, O. B. Vitrik, Yu. N. Kulchin, V. V. Zhakhovsky, and N. A. Inogamov, JETP Lett. **104**, 759 (2016).
87. D. Ofte, J. Nucl. Mater. **22**, 28 (1967).

Translated by K. Shakhlevich